

1 **Elucidating large-scale atmospheric controls on Bering**  
2 **Strait throughflow variability using a data-constrained**  
3 **ocean model and its adjoint**

4 **An T. Nguyen<sup>1\*</sup>, Rebecca A. Woodgate<sup>2</sup>, and Patrick Heimbach<sup>1</sup>**

5 <sup>1</sup>University of Texas at Austin, Austin, TX, USA

6 <sup>2</sup>University of Washington, Seattle, WA, USA

7 **Key Points:**

- 8 • An adjoint sensitivity analysis is performed to quantify the role of atmospheric  
9 forcing on the variability of Bering Strait throughflow  
10 • Primary driver of the variability is the wind stress over the Bering Sea and Arc-  
11 tic shelves, on timescales matching shelf wave propagation  
12 • Impact of precipitation, although consistent with steric flow control, yield insignif-  
13 icant variability on monthly to interannual timescales

---

\*Oden Institute for Computational Engineering and Sciences, The University of Texas at Austin, Austin, TX, USA

Corresponding author: An T. Nguyen, [atnguyen@oden.utexas.edu](mailto:atnguyen@oden.utexas.edu)

## Abstract

A regional data-constrained coupled ocean-sea ice general circulation model and its adjoint are used to investigate mechanisms controlling the volume transport variability through Bering Strait during 2002 to 2013. Comprehensive time-resolved sensitivity maps of Bering Strait transport to atmospheric forcing can be accurately computed with the adjoint along the forward model trajectory to identify spatial and temporal scales most relevant to the strait’s transport variability. The simulated Bering Strait transport anomaly is found to be controlled primarily by the wind stress on short time-scales of order 1 month. Spatial decomposition indicates that on monthly time-scales winds over the Bering and the combined Chukchi and East Siberian Seas are the most significant drivers. Continental shelf waves and coastally-trapped waves are suggested as the dominant mechanisms for propagating information from the far field to the strait. In years with transport extrema, eastward wind stress anomalies in the Arctic sector are found to be the dominant control, with correlation coefficient of 0.94. This implies that atmospheric variability over the Arctic plays a substantial role in determining Bering Strait flow variability. The near-linear response of the transport anomaly to wind stress allows for predictive skill at interannual time-scales, thus potentially enabling skillful prediction of changes at this important Pacific-Arctic gateway, provided that accurate measurements of surface winds in the Arctic can be obtained. The novelty of this work is the use of space and time-resolved adjoint-based sensitivity maps, which enable detailed dynamical, i.e. causal attribution of the impacts of different forcings.

## Plain Language Summary

An ocean circulation model, that was adjusted to match observations, is used to investigate what are the important factors controlling the oceanic flow of water through the Bering Strait. Results show that the flow through the strait is related to surface atmospheric winds over the Bering Sea Shelf (south of the strait) and the near coastal regions of the Arctic Ocean (north of the strait). In the model, knowledge of these winds over the preceding 1 month allows us to reconstruct most of the changes in the flow through the strait. A somewhat surprising result is that winds in the Arctic have a greater influence on the amount of water flowing through the Bering Strait than winds over any region of the Pacific Ocean or the Bering Sea. The connection between the winds and the flow through the strait is strong enough that interannual changes in the winds may be used to predict interannual change in the flow. This predictive skill opens up the prospect for an improved understanding of the causes and mechanisms of flow changes at this important Pacific-Arctic gateway, provided that accurate measurements of surface winds over the Arctic can be obtained.

## 1 Introduction

The narrow ( $\sim 85$  km wide) and shallow ( $\sim 50$  m deep) Bering Strait is the only oceanic connection between the Pacific and the Arctic oceans (Fig. 1a). The annual mean flow is about 0.8 Sv ( $1 \text{ Sv} = 10^6 \text{ m}^3/\text{s}$ ), northward through the strait, with a seasonal cycle ranging from  $\sim 0.4$  Sv to 1.4 Sv, and with significant interannual variability (Woodgate et al., 2005a, 2006, 2012). The Pacific waters carried by the flow (typically fresher than most Arctic waters, and seasonally warm and cold) contribute significantly to the stratification, as well as the heat, freshwater and nutrient budgets of the Chukchi Sea and the Arctic Ocean (e.g. Woodgate et al., 2005b; Serreze et al., 2006, 2007, 2016; Walsh et al., 1997; see Woodgate et al., 2015 and Woodgate, 2018 for reviews.) The Pacific Waters eventually exit the Arctic into the North Atlantic via the Fram Strait, Nares Strait, and the Canadian Arctic Archipelago, thus influencing the world ocean circulation (e.g. De Boer & Nof, 2004a, 2004b; Hu & Meehl, 2005; Hu et al., 2012; for a review, see Wadley & Bigg, 2002). Closer to the source, within the Chukchi Sea and possibly the western Arctic Ocean,

the inflow of warm Pacific waters is shown to influence sea-ice retreat (Woodgate et al., 2010; Serreze et al., 2016). This in turn affects light availability in the water column on the Chukchi Shelf, which, in combination with nutrient supply, may modulate regional in-ice (Arrigo, 2014) and under-ice (Arrigo et al., 2012) ecosystem activity.

Given the influential role of the Bering Strait throughflow, and its potential societal impacts (e.g., driving changes important for Arctic residents, and industrialization, such as resource exploitation and Arctic shipping/fishing), it is important to quantify the properties of the flow and, where possible, understand the mechanisms controlling how those properties change. Year-round in situ observations in the strait have been obtained nearly continually since 1990 (see Woodgate et al., 2015 for a review) and have indicated significant increases in volume ( $\sim 0.6$  to  $1.1$  Sv), heat and freshwater transports at least from the early 2000s to 2018 (Woodgate et al., 2015; Woodgate, 2018, Woodgate, unpublished data). To date, however, the causes for these changes remain poorly understood.

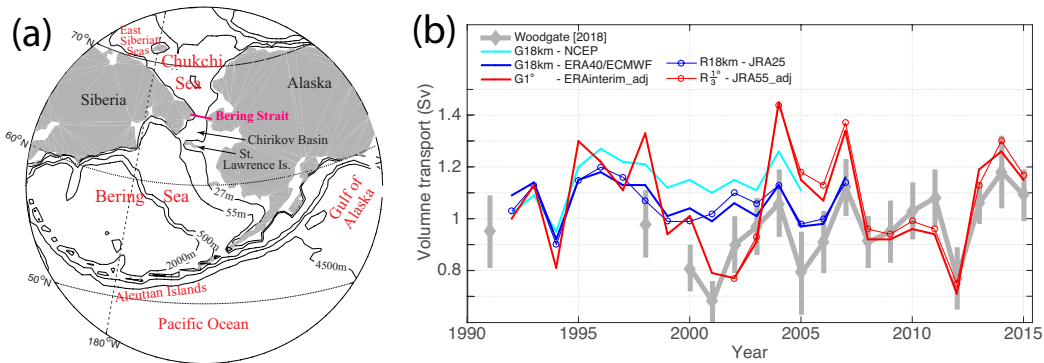


**Figure 1.** (a) Geographic location of the Bering Strait, showing bathymetric contours from the global ECCO version 4 configuration. (b) Annual mean northward volume transport through Bering Strait, estimated from various sources: in situ moorings observations (including a standard correction for the Alaskan Coastal Current, thick grey, with error bars, Woodgate, 2018); global (G, thick color lines) and regional (R, thin color lines with symbol) ECCO configurations using various atmospheric reanalyses and model horizontal grid resolutions (given in legend). The atmospheric reanalyses are NCEP/NCAR (Kalnay et al., 1996), ERA-40/ECMWF (Uppala et al., 2005), JRA25 (Onogi et al., 2007), ERA-Interim (Dee et al., 2011), and JRA55 (Kobayashi et al., 2015). Simulations marked with extension “adj” are from adjoint-based optimization, where the atmospheric forcing fields have been adjusted within their respective uncertainties to bring the model into agreement with satellite and in situ observations, including Bering Strait mooring data (Forget et al., 2015; Fenty et al., 2015).

The flow through the Bering Strait is typically conjectured to be associated with large scale oceanic “pressure head” forcing (usually cited as the difference in sea surface height between the Pacific and the Arctic oceans), modified by local wind forcing within the strait (see Woodgate et al., 2005b; Woodgate, 2018 for discussion). This hypothesis was first discussed in the international literature by Coachman and Aagaard (1966), a work which summarized prior Russian studies in the region, and, as other authors, tacitly assumed the pressure head forcing to be quasi constant in time. While the hourly variability of the throughflow is extremely well correlated with the local wind (correlation coefficient  $\rho \sim 0.8$ ), longer term variability is not well explained by variations in the local wind, leading to the suggestion that seasonal to interannual change relates to

88 variability in the pressure head drivings of the flow (Woodgate et al., 2010, 2012; Woodgate,  
89 2018; Peralta-Ferriz & Woodgate, 2017).

90 The details of this pressure head forcing, however, have long remained unclear. The  
91 origin of the pressure head itself has been suggested to be either steric (Stigebrandt, 1984;  
92 Steele & Ermold, 2007) or driven by global winds (e.g. De Boer & Nof, 2004a, 2004b).  
93 More recently, using a conceptual model, Danielson et al. (2014) correlated wind, pres-  
94 sure, and sea surface height north and south of the strait with the throughflow and sug-  
95 gested that the Bering shelf circulation is highly controlled by basin scale wind patterns,  
96 particularly the Aleutian Low in the Bering Sea/Gulf of Alaska, with additional contri-  
97 butions from the Beaufort and Siberian Highs and modifications from coastal shelf waves.  
98 Kawai et al. (2018) also find relationships between model sea surface heights in the north-  
99 east Bering Sea and the southwest Chukchi Sea with the flow through the Bering Strait.  
100 Yet more recent work (Peralta-Ferriz & Woodgate, 2017) finds high correlations (cor-  
101 relation coefficient  $\rho \sim 0.6$ ) between monthly flow variability and a specific pattern of  
102 ocean bottom pressure (OBP), viz a pattern dominated by low OBP in the East Siberian  
103 Sea (assisted in winter by high OBP over the Bering Sea Shelf). Although that study  
104 excludes interannual changes, it suggests a mechanism whereby westward Arctic coastal  
105 winds invoke northward Ekman transport over the East Siberian Sea, enhancing the sea-  
106 level difference between the Pacific and the Arctic and thus reducing sea level in the East  
107 Siberian Sea and drawing flow northward through the strait. In contrast to prior work,  
108 Peralta-Ferriz and Woodgate (2017) suggest the monthly variability of the flow to be pri-  
109 marily driven by Arctic processes, not Bering Sea processes.

110 All of the above mentioned studies, however, are based on either simple theoret-  
111 ical or statistical models. While these approaches may suggest possible connections, they  
112 do not prove causality, nor do they expose underlying dynamical mechanisms. The com-  
113 plexity of the system suggests that progress on understanding the large-scale mechanism  
114 controlling throughflow variability may be made by drawing on the much more complete  
115 numerical simulations of coupled sea ice-ocean general circulation models. In particu-  
116 lar, we will utilize the non-linear inversion (“adjoint”) framework established within the  
117 global ECCO (Estimating the Circulation and Climate of the Ocean) version 4 coupled  
118 ice-ocean configuration (Forget et al., 2015; Heimbach et al., 2019), which is based on  
119 the Massachusetts Institute of Technology general circulation model (MITgcm, Marshall  
120 et al., 1997; Adcroft et al., 2018) and its adjoint.

121 Unlike a perturbation simulation that quantifies the impact of the change of *one*  
122 *input* on *all outputs* (directional derivative information), the adjoint model simulation  
123 quantifies the sensitivity of *one output* to *all inputs* (gradient information). The adjoint  
124 model provides a dynamical, i.e., causal link between the changed output quantity of in-  
125 terest, such as the transport through the Bering Strait, and the inputs. Algorithmic dif-  
126 ferentiation implements the adjoint, which formally represents the transpose of the lin-  
127 earized model operator, on an elementary line-by-line basis using the chain and prod-  
128 uct rules of differentiation. The transpose amounts to a time-reversal of information flow,  
129 i.e., the resulting adjoint model propagates the change of one output back in time to as-  
130 sess its sensitivity to changes in all inputs. With this framework, the flow of informa-  
131 tion, e.g., sensitivity of the transport to the forcings, can be tracked from Bering Strait  
132 back to its sources in space and time (Heimbach et al., 2010; Fukumori et al., 2015; Pil-  
133 lar et al., 2016). Compared to purely statistical approaches (e.g., lag correlations or em-  
134 pirical orthogonal function decomposition), the adjoint approach, being based on the nu-  
135 merical model dynamics, provides a robust causal description. It elucidates mechanisms  
136 driving the variability and allows for the assessment of time-lagged influences.

137 For this study, we considered several adjoint model configurations ranging from global  
138  $1^\circ$  to regional  $1/3^\circ$  resolution prior to choosing the ECCOv4 configuration. The narrow-  
139 ness and shallowness of the Bering Strait suggest that a regional high resolution model  
140 configuration would be more appropriate than a global and coarser resolution one. In

141 practice, however, we have consistently observed that, in the global MITgcm simulations  
142 (i.e., those which do not prescribe a set flow through the Bering Strait), a variety of model  
143 resolutions and wind forcing all produce similar, roughly 1 to 1.1 Sv annual mean north-  
144 ward flow through the Bering Strait (Fig. 1). While at smaller grid spacings the local  
145 circulation in the Bering and Chukchi Seas becomes more detailed, we do not encounter  
146 any systematic change in the total volume of the throughflow with increasing resolution.  
147 In addition, when a regional configuration (R) takes lateral boundary conditions from  
148 a global configuration, the Bering Strait transport is largely determined by the imposed  
149 lateral boundary conditions, irrespective of regional surface atmospheric forcing. This  
150 is evidenced in the similarity between the R1/3° run with JRA55 forcing (red line with  
151 symbol), which takes lateral boundary conditions from the global G1° run with ERA-  
152 Interim (red line) or R18km which used JRA-25 as forcing (blue line with symbol, Nguyen  
153 et al., 2011; Kinney et al., 2014), and the global run G18km from the ECCO2 project  
154 with ERA40 /ECMWF (blue line). Despite differences in atmospheric forcings, horizon-  
155 tal resolutions, treatment of dissipation and friction (ECCO2 models use Leith viscos-  
156 ity and free-slip boundary friction, ECCOv4r2 uses harmonic viscosity and no-slip bound-  
157 ary friction), and assimilation procedure (ECCO2 is restricted to a low-dimensional Green’s  
158 functions based parameter calibration, ECCOv4r2 uses an adjoint-based state and pa-  
159 rameter estimation approach), all models show low transports in 1994, 1999–2003, 2005,  
160 and high transports in 1995–1996, 2004, and 2007. All these reasons, in addition to com-  
161 putational efficiency, point to a global configuration at 1° as a sufficient choice for in-  
162 vestigating large-scale controlling mechanisms for the Bering Strait transport variabil-  
163 ity in our study.

164 In general, the ensemble of model simulations, which use a variety of atmospheric  
165 forcings, encompasses the range of the observed transports, although there are differences  
166 in year-to-year variations and in long term trends, which show increasing flow in the ob-  
167 servational data (Woodgate, 2018). For example, comparison between simulated and ob-  
168 served Bering Strait transport interannual trends show more consistency for the period  
169 2008–2015 (simulated: 0.04 Sv/yr, observed: 0.03 Sv/yr, correlation coefficient: 0.9) than  
170 for the period 2004–2012 (simulated: -0.07 Sv/yr, observed: 0.01 Sv/yr, correlation co-  
171 efficient: 0.2). The latter discrepancy between simulations and data is largely due to the  
172 anomalously high transport in 2004 and low transport in 2011, seen more extremely in  
173 the models than in the data. Nevertheless, we emphasize that the focus of this study is  
174 not on attempting to strictly reproduce the observed Bering Strait transport time-series  
175 over the decades. Instead, our goal is to deconstruct the time-series of the state estimate  
176 to identify the dominant regions, physical processes, and time-scales that control flow  
177 variability in the underlying dynamical model. Such information may then be used to  
178 understand possible causes of real world change and identify reasons for discrepancies  
179 between the models and the observations.

180 This paper is organized as follows. Section 2 describes the model configurations,  
181 the adjoint sensitivity experiments by which the sensitivity of the Bering Strait trans-  
182 port to various input atmospheric forcings are computed, and the procedure by which  
183 we then use these sensitivities to reconstruct the transport anomalies. Section 3 inves-  
184 tigate the spatial and temporal patterns of the adjoint sensitivities and quantifies the  
185 contributions of atmospheric forcings at various time-scales (interannual, seasonal, and  
186 sub-monthly) to the Bering Strait transport. Section 4 discusses the regions found to be  
187 most influential on the variability of the throughflow and the underlying physical mech-  
188 anisms. In addition, it considers the role of precipitation as the steric driving mechanism  
189 of the Bering Strait transport variability. The transport extrema between 2004–2007 seen  
190 in the model are also discussed. Section 5 summarizes the key findings.

## 2 Methodology

### 2.1 Model description

The ECCO version4 release 2 (ECCOv4r2) global ocean-sea ice state estimate at nominally 1 degree horizontal resolution (Forget et al., 2015; Fukumori et al., 2018) is the primary modeling tool in this study. The term “state estimate” here refers to the result of a data assimilation procedure by which a general circulation model is fit, in a least-squares sense, to a wide range of observations. The observational constraints used for the assimilation in ECCOv4r2 include as many ocean and sea ice observations as available and practical, including satellite sea surface heights and temperature, sea ice concentration from Special Sensor Microwave/Imagers (SSM/I, Cavalieri et al., 1991), Argo floats (Roemmich et al., 2009), Ice Tethered Profilers (Toole et al., 2006), and moorings at important Arctic and Nordic Seas gateways (see Forget et al., 2015 for a complete list). Note that Bering Strait mooring data have been included as a constraint. Unlike in “re-analyses”, the assimilation procedure is such that the underlying conservation laws as expressed by the governing equations for momentum and tracers are strictly enforced, thus enabling accurate analyses of budgets and causal mechanisms (Stammer et al., 2016; Wunsch & Heimbach, 2007, 2013).

We summarize here only the salient features of the configuration that are relevant for our investigation. A more thorough description of ECCOv4r2 can be found in Forget et al. (2015) and Fukumori et al. (2018). The full period of ECCOv4r2 is 1992–2013. The choice of length of an adjoint sensitivity run within this period does not need to match that of ECCOv4r2. Instead it is guided by the time-scales of interest of the physical processes being studied. For this work we choose a shorter period of 01/Jan/2002–31/Dec/2013 to allow us to look at sensitivity **at lag time** varying from 1 hour to 12 years. Our results show that this length of study is likely sufficient, as our dynamical reconstruction recovers a high fraction of explained variance observed by timescales much shorter than 12 years. The initial conditions for our study come from the ocean and sea ice state of ECCOv4r2 on 01/Jan/2002. The surface atmospheric forcing come from the ECCOv4r2 adjusted ERA-Interim fields for 2002–2013, as described in Forget et al. (2015). The model is also forced with monthly-mean estuarine runoff, which are based on the Regional, Electronic, Hydrographic Data Network for the Arctic Region (R-ArcticNET) dataset (Lammers & Shiklomanov, 2001; Shiklomanov et al., 2006).

The grid spacing at the Bering Strait is  $\sim 48$  km in the horizontal and 10 m in the vertical. Although this gives only two grid points across the Bering Strait, as shown in Fig. 1b, the total transport at the strait is very similar to that in the high resolution models. The model uses a non-energy-conserving semi-implicit time-stepping algorithm to solve for the free surface elevation (Marshall et al., 1997) in rescaled  $z^*$  coordinates (Adcroft & Campin, 2004) with a non-linear free surface capability and real freshwater flux boundary condition (Campin et al., 2004).

Prior studies show that this semi-implicit method can damp gravity wave amplitudes by up to 50% and reduce phase speeds by up to 35% within one cycle (Kurihara, 1965; Casulli & Cattani, 1994; Campin et al., 2004). In addition, wavelengths and phase speeds can be further modified for unresolved baroclinic shelf and coastally trapped Kelvin waves in coarse grid resolution models with added friction (Hsieh et al., 1983; Griffiths, 2013), especially when the model coastline is not aligned with the C-grid orientation (Schwab & Beletsky, 1998; Griffiths, 2013). For ECCOv4r2, the use of partial cells to represent topography (Adcroft et al., 1997) alleviates some of the grid-resolution related problems. However, in combination with added horizontal and vertical friction, the model’s representation of theoretical Kelvin and coastal shelf waves are modified numerical equivalents and should be interpreted with caution. This applies to “reverse Kelvin wave” propagation in the adjoint model as much as it applies to the full nonlinear forward model.

As such the adjoint model exposes these adjustment processes and may help to uncover how adjustment to external forcing is conveyed in the model being studied.

The configuration used in this study utilizes the adjoint capability developed within the ECCO consortium (Wunsch & Heimbach, 2007, 2013) but with several approximations described in Forget et al. (2015). The coupled ocean-sea ice adjoint model has been generated by means of algorithmic differentiation (Heimbach et al., 2010; Fenty & Heimbach, 2013). Model-data misfits are reduced systematically through gradient-based iterative minimization of a least-squares misfit function (adjoint or Lagrange Multiplier method) by adjusting model parameters and input fields (together termed “control variables”), which carry sizable uncertainties (Forget et al., 2015; Stammer, 2005; Fenty & Heimbach, 2013).

As described in Forget et al. (2015), for ECCOv4r2, the linearization of the sea ice model and the mixed-layer parameterization represented in the adjoint model contains several approximations. One way to assess the impact of these simplifications in the adjoint model is to quantify how well a propagating perturbation that is simulated with the full nonlinear forward model can be reconstructed from the adjoint gradients with the reduced physics in a Taylor series expansion. As shown in Section 3, the reconstructed time-series of transport anomalies based on the linearized (and approximated) adjoint sensitivity can capture very well the transport anomalies obtained from forward model that used the full physics. This indicates that the impact of these reduced linearized physics in the adjoint model is small for the Bering Strait transport problem.

For the current study, similar to ECCOv4r2, the control variable space  $\Omega$  is comprised of the two components of the surface momentum fluxes, 10-m east- and north-ward wind stresses, as well as five surface atmospheric variables: precipitation, downward short- and long-wave radiation, surface specific humidity, and 10-m air temperature. Uncertainties for these control variables are described in Fenty and Heimbach (2013) and Chaudhuri et al. (2013, 2014). Although runoff and evaporation are not part of the control space, in practice they project onto the precipitation sensitivities, interpreted as linear combination of net freshwater fluxes.

## 2.2 Adjoint sensitivity and reconstruction

The forward and adjoint models can be used to assess how variability in the surface atmospheric forcings influence the flow through the Bering Strait by the following procedure. The model is first integrated forward in time from 2002–2013. The mean Bering Strait volume transport at a time  $t$ ,  $J(t)$  over a period  $T$  starting from any given time  $t - T/2$  is defined as:

$$J(t) \equiv \frac{1}{T} \int_{t-T/2}^{t+T/2} \int_A \mathbf{u}(t') \cdot \hat{\mathbf{n}} \, dA \, dt' \quad (1)$$

where  $\mathbf{u}$  is the time-varying 2-D horizontal velocity vector field on a vertical section across the strait, and  $A$  is the cross-sectional area of the strait whose normal component is  $\hat{\mathbf{n}}$ . The anomaly  $\delta J$  is defined as  $J(t)$  minus the time-mean,  $\overline{J_{2002-2013}}$ , of our integration period of 2002–2013:

$$\delta J(t) \equiv J(t) - \overline{J_{2002-2013}} \quad (2)$$

The adjoint model computes sensitivities  $\partial J/\partial\Omega$  of  $J$  to all control variables that are part of the control vector  $\Omega$ . In the following we will interchangeably refer to these  $\partial J/\partial\Omega$  as “sensitivities”, “gradients”, “influences”, and “partial derivatives” as, dependent on the context, sometimes one term conveys the point in the discussion more clearly than the others. The gradients can be efficiently computed for a very high-dimensional con-

288 trol space via the adjoint method (Wunsch & Heimbach, 2007, 2013), i.e. one adjoint in-  
 289 tegration yields all partial derivatives  $\partial J/\partial\Omega_k$  simultaneously for each of the individual  
 290 surface atmospheric forcing variables  $\Omega_k$ . The gradients consist of two-dimensional sur-  
 291 face fields (in  $x_1, x_2$ ) and these derivatives are updated at regular (e.g., bi-weekly) in-  
 292 tervals (linearly interpolated in between) along the model temporal trajectory. Their spa-  
 293 tial and temporal patterns can be used to reconstruct (in the sense of a Taylor series ex-  
 294 pansion) the forward time-series of the throughflow **anomalies**  $\widetilde{\delta J}(t)$  as follows (Fukumori  
 295 et al., 2015; Pillar et al., 2016),

$$296 \quad \widetilde{\delta J}(t) = \sum_k \widetilde{\delta J}_k(t) = \sum_k \int_{t_0}^t \int_{x_1} \int_{x_2} \frac{\partial J}{\partial\Omega_k}(x_1, x_2, \alpha - t) \delta\Omega_k(x_1, x_2, \alpha) dx_1 dx_2 d\alpha \quad (3)$$

297 where  $\widetilde{\delta J}(t)$  is the reconstructed transport anomaly, with the  $\sim$  symbol added to distin-  
 298 guish it from the anomaly obtained from the forward run  $\delta J_{fwd}$ .  $t_0 = 01/\text{Jan}/2002$  is  
 299 the time when the model integration starts,  $\alpha$  is a time prior to the current time  $t$ , with  
 300 values thus ranging from  $t_0$  to  $t$ ,  $(\alpha - t)$  is the time-lag,  $\delta\Omega_k$  the atmospheric forcing  
 301 anomalies associated with the forcing field  $k$ , and  $\partial J/\partial\Omega_k(x_1, x_2, \alpha - t)$  gives the influ-  
 302 ence on  $\delta J$  of variable  $\delta\Omega_k$  at lag time  $\alpha - t$  and spatial location  $[x_1, x_2]$ .

303 For each  $k$ , the anomalies  $\delta\Omega_k$  are computed as the input forcings minus their re-  
 304 spective 2002–2013 mean,  $\delta\Omega_k(t) = \Omega_k(t) - \Omega_{2002-2013}$ . The peak-to-peak ranges of  
 305  $\delta\Omega_k$  come primarily from the seasonal cycles, with 90-percentile values of 0.15 N/m<sup>2</sup>, 0.12  
 306 N/m<sup>2</sup>, 17°C, 0.006 kg/kg, 185 W/m<sup>2</sup>, 87 W/m<sup>2</sup>, and  $8 \times 10^{-8}$  m/s for zonal and merid-  
 307 ional wind stresses, 2 m air temperature, specific humidity, downward short- and long-  
 308 wave radiation, and precipitation, respectively.

309 Eqn. (3) indicates that the anomaly  $\widetilde{\delta J}(t)$  at any time  $t$  is a convolution of the time-  
 310 lagged  $(\alpha - t)$  gradient  $\partial J/\partial\Omega$  with the forcing anomaly  $\delta\Omega$  at time  $\alpha$ . In simpler lan-  
 311 guage the equation states that the reconstructed anomaly  $\widetilde{\delta J}(t)$  is computed from the  
 312 sum of point-wise influences (in space and time) integrated over the time  $\alpha$ , which ranges  
 313 from  $t_0$  to the time  $t$  of consideration. To put this more simply still, the adjoint tech-  
 314 nique quantifies the influence of a forcing at a point in space on a quantity of interest  
 315 (here the Bering Strait transport) through anomaly propagation (usually in the form of  
 316 oceanic linear adjustment processes) at various time lags (here up to the length of our  
 317 model simulation, 12 years). This implies that contributions to the transport anomaly  
 318  $\delta J(t)$  at any time  $t$  will depend on how sensitive  $\delta J(t)$  is to each forcing anomaly  $\delta\Omega_k$   
 319 at various time-lags corresponding to prior days, months or years, and the spatial dis-  
 320 tribution of the sensitivity locally and away from the strait. Note that the time-lag  $(\alpha -$   
 321  $t)$  only takes on negative values, indicating that a past event has influence on a future  
 322  $\delta J$ . If the system is sufficiently linear, the reconstructed  $\widetilde{\delta J}(t)$  will be close to the full  
 323  $\delta J_{fwd}(t)$  obtained with the full nonlinear forward model.

324 Although in theory, being the derivative of a nonlinear operator,  $\partial J/\partial\Omega$  may vary  
 325 with the time when  $J$  is defined, a reasonable approximation is to assume that if there  
 326 is a dominant linear mechanism linking the drivers  $\delta\Omega$  with  $\delta J$ , then  $\partial J/\partial\Omega$  should be,  
 327 to first order, independent of the time when  $J$  is defined. Tests (see Supplemental Ma-  
 328 terial) show this to be the case, and thus in what follows, we use  $\partial J/\partial\Omega$  that correspond  
 329 to a  $J$  defined as the monthly mean Sept 2013 transports. This choice of  $J_{Sep/2013}$  is based  
 330 on the consideration that the September transports lie between the seasonal transport  
 331 extrema (Woodgate et al., 2005a) with maximum  $\delta J$  during the summer months and min-  
 332 imum  $\delta J$  during the winter months. With  $J$  defined as  $J_{Sep/2013}$ , we compute time-lagged  
 333 gradients  $\partial J/\partial\Omega$  at discrete, monthly intervals.

334 We will denote  $\frac{\partial J}{\partial\Omega(l)}$ , where  $l = \{1, 2, \dots\}$  months, as the monthly mean sensi-  
 335 tivity spanning the time range  $[l-1, l)$  months, and refer to this quantity as  $l$ -month

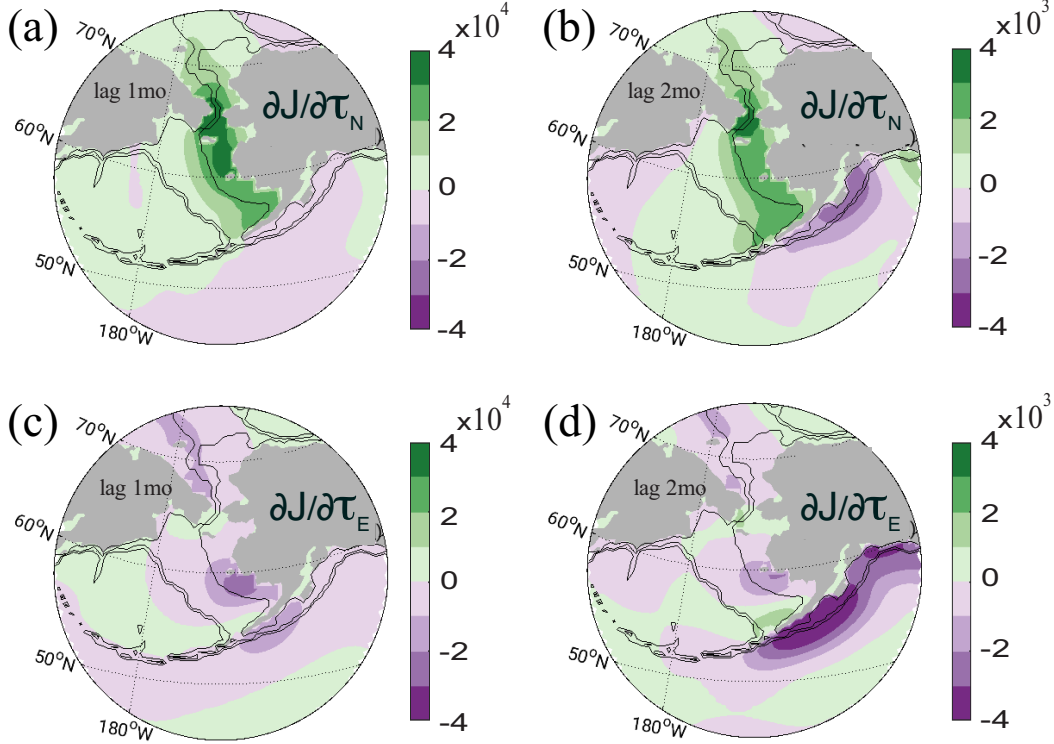


**Figure 2.** Sensitivity of Bering Strait volume transport anomalies to increments in (a–b) northward wind stress  $\frac{\partial J}{\partial \tau_N}$  and (c–d) eastward wind stress  $\frac{\partial J}{\partial \tau_E}$  in units of  $(m^3/s)/(N/m^2)$  at (a,c) 1-month and (b,d) 2-month lags (see Section 2.2 and eqn (3) for the definition of lag.) A positive gradient here implies that a positive increment  $\delta \tau_{E,N}$  will result in a positive increase in the  $\tilde{\delta J}$  with magnitude as indicated in the color scales and units. The highest sensitivity of order  $10^4$   $(m^3/s)/(N/m^2)$  is found for  $\frac{\partial J}{\partial \Omega(1)}$ , i.e., within the 1-month lag. It is highly localized to the Bering Strait and shallow Bering and Chukchi Sea shelves. Bathymetric contours are the same as shown in Fig 1a.

336 lag sensitivity. For example, the 1-month lag sensitivity,  $\frac{\partial J}{\partial \Omega(1)}$ , is the time average over  
 337 all sensitivities from lag zero to lag 1 month. These monthly mean sensitivities are 2D  
 338 surface fields.

### 3 Results

#### 3.1 Adjoint sensitivity maps

341 Monthly average adjoint sensitivities were computed for all seven atmospheric control  
 342 variables at different monthly-averaged lag times. The largest influence found was  
 343 related to surface wind stress. Sensitivities with respect to meridional (N) and zonal (E)  
 344 wind stress  $\frac{\partial J}{\partial \tau_N}$  and  $\frac{\partial J}{\partial \tau_E}$  are highest at 1-month lag, and both wind stress components  
 345 contribute significantly to  $\delta J(t)$  (Fig. 2).

346 The largest sensitivities are found in the strait itself, with  $\frac{\partial J}{\partial \tau_N}$  being approximately  
 347 (in magnitude) two times larger than  $\frac{\partial J}{\partial \tau_E}$ . This is consistent with previous observation-  
 348 based results that the northward flow through the strait is best correlated with the wind  
 349 at heading  $330^\circ$  (Woodgate et al., 2005b). Away from the strait, the largest sensitivi-

350 ties are found over the shallow shelves south and north of the strait, especially the Bering  
 351 Sea Shelf above 500 m (for northward wind stress), the Gulf of Alaska, the Chukchi Sea,  
 352 and the East Siberian Sea shelf break. Within these regions, over the northern Bering  
 353 Sea Shelf between 0–150 km south of the strait,  $\tau_N$  has the strongest impact on the strait  
 354 transport at up to 1-month lag, with positive wind change over the Bering Sea Shelf re-  
 355 sulting in positive increase in Bering Strait transport (see the range in the color-scale  
 356 in Fig. 2a). The combination of positive  $\partial J/\partial\tau_N$  and negative  $\partial J/\partial\tau_E$  parallel to and  
 357 between the Alaskan coast and the 500 m isobath in the Bering Sea implies that north-  
 358 westward wind stress here promotes positive  $\delta J$ , likely via a mechanism of onshelf trans-  
 359 port.

360 Away from the strait, there exist several regions with significant influences as well.  
 361 In particular, southeast of the Aleutian islands, negative  $\partial J/\partial\tau_N$  and  $\partial J/\partial\tau_E$  along the  
 362 Alaskan coast and the Aleutian Islands suggest that southwestward wind stress in this  
 363 region promotes the strengthening of the Alaska Coastal Current (Weingartner et al.,  
 364 2005), leading to enhanced northward flow through the Aleutian Islands onto the Bering  
 365 Shelf and also increasing  $\delta J$  at the Bering Strait at lags of 1–2 months. These results  
 366 are consistent with statistical wind-to-transport correlations of Danielson et al. (2014).

367 Inside the Arctic, positive  $\partial J/\partial\tau_N$  and negative  $\partial J/\partial\tau_E$  indicate northwestward  
 368 wind stress anomalies in the Chukchi and East Siberian Seas promote  $\delta J$  increases. The  
 369 likely mechanisms are those suggested by Peralta-Ferriz and Woodgate (2017), who find  
 370 significant correlations between westward winds along the East Siberian Sea shelf break  
 371 and the flow through the Bering Strait, especially with the component of the flow not  
 372 associated with the local wind (i.e., the pressure head term, Woodgate, 2018). Peralta-  
 373 Ferriz and Woodgate (2017) propose a mechanism by which these westward winds in the  
 374 Arctic move waters off the East Siberian Sea shelf via Ekman processes, lowering sea level  
 375 in the East Siberian Sea, and generating a pressure gradient that enhances northward  
 376 flow of waters through the strait (as per the theory of flow through a rotating channel,  
 377 see e.g., Toulany & Garrett, 1984). These regions (both south and north of the strait)  
 378 are suggested areas of formation of shelf waves that may contribute to driving Bering  
 379 Strait transport anomalies (Danielson et al., 2014). Section 4 discusses in more detail  
 380 shelf waves as a mechanism for propagation of sensitivities to the Bering Strait.

381 At a 2-month time lag, sensitivities drop approximately one order of magnitude,  
 382 and are spread further north and south of the strait (Fig. 2b,d). All patterns and signs  
 383 of  $\partial J/\partial\tau_{E,N}$  remain consistent with those within the 1-month lag. Additional features  
 384 include those further south along the western Canadian coast, where an increase in north-  
 385 westward wind stress promotes a positive  $\delta J$  at the strait two months later. Within the  
 386 Arctic, southwestward wind stress anomalies in the Kara Sea and much further away in  
 387 the eastern Nordic Sea (both not shown) also appear to have some influence on the Bering  
 388 Strait throughflow, although the magnitudes of sensitivity is significantly reduced such  
 389 that their overall contribution to  $\delta J$  is negligible (see further discussion in Section 3.4).

390 After two months, the sensitivities decrease by another factor of 5–10, such that  
 391 their contribution to the transports is insignificant (not shown).

### 392 3.2 Reconstruction of transport anomaly time series

393 To investigate the main driver of the throughflow variability at Bering Strait in the  
 394 model, we reconstruct the transport anomaly time series by summing the contributions  
 395 from  $\partial J/\partial\Omega$  globally, following eqn. (3). Fig. 3 shows  $\delta J_{fwd}$  obtained from the model  
 396 forward run (black) and  $\widetilde{\delta J}$  from the reconstruction via eqn. (3) (red, blue). Two recon-  
 397 structions were made, one using only contributions from the northward and eastward wind  
 398 stress anomalies (blue in Fig. 3) for the purpose of isolating the role of winds, and one  
 399 using contributions from all seven atmospheric forcing fields (red) for the purpose of as-  
 400 sessing the role of the non-wind stress terms. Also shown are the correlation coefficient

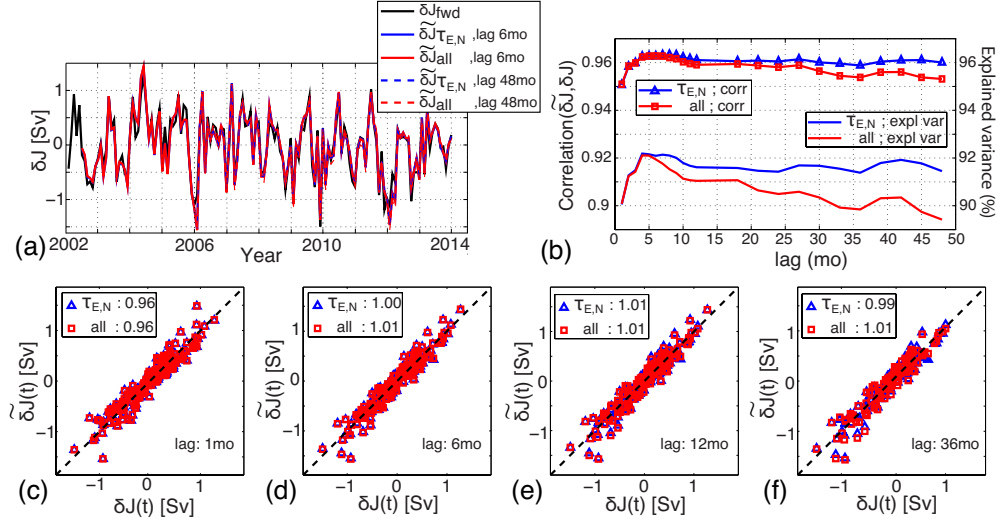


**Figure 3.** (a) Time series of  $\widetilde{\delta J}(t)$  reconstructed using anomalies of either only wind stress (blue) or all seven atmospheric components of  $\Omega$  (red), to be compared with the forward time series  $\delta J_{fwd}(t)$  in black. (b) Correlation coefficient  $\rho$  between  $\widetilde{\delta J}$  (the reconstructed transport anomalies) and  $\delta J_{fwd}$  (the transport anomalies from the forward model; lines with symbols), along with percentage of explained variance (PEV, line without symbols, using y-axis to the right) for reconstructions which are cumulatively summed over the range of lags indicated in the abscissa. See Section 3.3 for discussion on the degradation of  $\rho$  and PEV when all atmospheric forcing terms are used in the reconstruction. (c–f) Scatter plots of the the forward  $\delta J_{fwd}$  with full model dynamics versus the reconstructed time series  $\widetilde{\delta J}$  for lags of up to (c) 1 month, (d) 6 months, (e) 12 months, and (f) 36 months. Numbers in the legend indicate the slope of the fitted line, with the one-to-one line shown in dashed black for reference.

401  $\rho$  and percentage of explained variance (PEV) between the forward and reconstructed  
 402 time series. The contribution from the wind components (blue curve in Fig. 3a) is al-  
 403 most identical to (and thus on the plot almost completely overwritten by) the contribu-  
 404 tion from all components (red curve) indicating that the non-wind components have a  
 405 very small effect.

406 The reconstructed time series  $\widetilde{\delta J}_{all}$  (red) correlates strongly ( $\rho > 0.94$ ) with the  
 407 forward model time series  $\delta J_{fwd}$  (black) at all time lags (Fig. 3c–f), with slopes in the  
 408 scatter plots of  $\widetilde{\delta J}_{all}$  versus  $\delta J_{fwd}$  ranging between 0.96 and 1.01. This suggests that the  
 409 reconstruction captures nearly the full dynamics of the strait transport anomalies simu-  
 410 lated with the forward model. The reconstruction using only the 1 month lag contribu-  
 411 tion still captures  $\sim 90\%$  of the variability and 96% of the magnitude (slope on scatter  
 412 plot). The wind stress components are the dominant contributors to the transport  
 413 anomalies at monthly to multi-year time-scales, with all other atmospheric forcing terms  
 414 contributing only  $\sim 1\text{--}2\%$  (compare the slope of “all” versus  $\tau_{E,N}$  in Fig. 3c–f).

415 A noticeable degradation of  $\rho$  and PEV when including contributions from longer  
 416 time lags can be seen when all forcing terms are included (Fig. 3b). A breakdown of con-  
 417 tributions from individual forcing terms shows that the terms associated with heat fluxes  
 418 (e.g., air temperature, downward long and short waves) contribute approximately equally  
 419 to the degradation (not shown). We speculate that these terms may have an accumu-  
 420 lated non-linear effect on the water column with time that the adjoint sensitivities can-  
 421 not fully capture due to some of the simplified physics in the adjoint model, as discussed

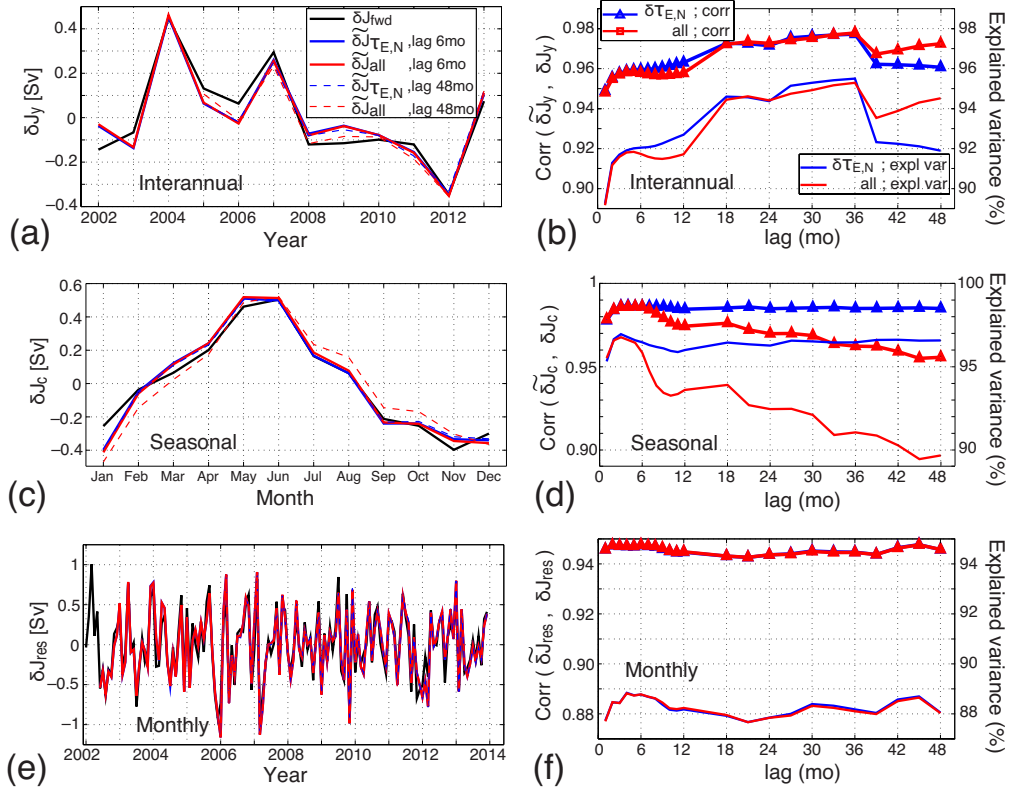


**Figure 4.** Decomposition of the forward model  $\delta J_{fwd}(t)$  and reconstructed  $\widetilde{\delta J}(t)$  into their annual mean (a), 12-mo climatology (or seasonal, c), and monthly (or high-frequency, e). Left panels (a,c,e) show the time series of each component, while right panels (b,d,f) show correlation  $\rho$  and percentage of explained variance (PEV) between the reconstructed  $\widetilde{\delta J}$  and the model forward  $\delta J_{fwd}$  time series for annual (b), seasonal (d) and monthly (f). See text for discussion on the degradation of  $\rho$  and PEV when all atmospheric contribution terms are included in the reconstruction of the climatological time series in (d).

422 in Section 2. As a result, errors in  $\widetilde{\delta J}$  are aggregated with increasing cumulative lags the  
 423 further back in time the reconstruction is carried out. This degradation in the reconstruc-  
 424 tion due to contributions from buoyancy terms remains insignificant after 36 months, with  
 425 correlation coefficients and explained variance still above 0.95 and 0.9 (Fig. 3b). It has  
 426 also been observed in previous adjoint-based reconstructions (see Pillar et al., 2016; Smith  
 427 & Heimbach, 2018), but a full investigation of whether the degradation is due to inac-  
 428 curacies in the approximated adjoint model or missing physics in the forward model is  
 429 beyond the scope of this study. Excluding the contributions from air temperature and  
 430 downward radiation, the correlation between the  $\widetilde{\delta J}$  reconstructed using wind stress and  
 431  $\delta J_{fwd}$  remain steady when longer time lags are considered, suggesting that there is a close  
 432 correspondence between the wind stress and the Bering Strait transport anomalies, and  
 433 that the effect of winds has a short time history (Fig. 3f). Finally, adding the contribu-  
 434 tion from precipitation to  $\widetilde{\delta J}$  (not shown) did not change the correlation significantly.

### 435 3.3 Decomposing $\widetilde{\delta J}(t)$ into temporal components

436 To examine short-to-long time-scale contributions, the time series of monthly trans-  
 437 port anomaly from both the forward model  $\delta J_{fwd}$  and the adjoint-based reconstruction

438  $\widetilde{\delta J}(t)$  can alternatively be decomposed into its monthly (sub-seasonally), seasonally (12-  
 439 month climatology), and multi-year components (Fig. 4). We calculate this discretely,  
 440 rather than as a spectral decomposition as our time series is comparatively short. For  
 441 any time series of anomalies, the decomposition is done as follows. The 2002–2013 an-  
 442 nual mean time series (12 annual means), denoted by subscript “ $y$ ”, is obtained by com-  
 443 puting the average of the anomaly for each calendar year. The monthly climatology time  
 444 series (12 monthly means), denoted by subscript “ $c$ ”, is computed by subtracting from  
 445 each monthly value the annual average for that year, and then averaging over each month  
 446 for the entirety of the record. Finally, the “residual”, denoted by subscript “ $res$ ”, is com-  
 447 puted by subtracting from each monthly anomaly both the annual mean and the sea-  
 448 sonal climatology for that month. The decomposition described above operates strictly  
 449 on the transport anomaly time-series  $\delta J_{fwd}$  or  $\widetilde{\delta J}$ . Note that  $\widetilde{\delta J}$  is obtained from eqn. (3)  
 450 using the total (i.e., non-decomposed) forcing anomalies  $\delta\Omega$ .

451 Given the dominance of wind stress forcing on  $\delta J$  at short lags (Section 3.2), we  
 452 explore a second approach for the temporal decomposition that would allow us to relate  
 453 directly the temporally decomposed forcings  $\delta\Omega_{[y,c,res]}$  to the decomposed  $\widetilde{\delta J}_{[y,c,res]}$  as  
 454 follows:

$$455 \quad \widetilde{\delta J}_{[y,c,res]}(t) \approx \int_{t_0}^t \int_{x_1} \int_{x_2} \frac{\partial J}{\partial \Omega_k}(x_1, x_2, \alpha - t) \delta\Omega_{[y,c,res],k}(x_1, x_2, \alpha) dx_1 dx_2 d\alpha \quad (4)$$

456 A comparison of these two approaches (i.e., a decomposition obtained from the full  
 457 reconstructed  $\widetilde{\delta J}$  and that obtained from approximation following eqn. 4) can be found  
 458 in the Supplemental Material. It shows that both methods yield approximately the same  
 459 results. The important advantage of performing the reconstruction following the approx-  
 460 imate method of eqn. (4) is that it is then straightforward to calculate, for example, the  
 461 interannual transport anomalies,  $\widetilde{\delta J}_y$ , from the interannual forcing anomalies,  $\delta\Omega_y$ , of  
 462 any forcing reanalysis. In the following, all reconstructed decompositions were obtained  
 463 using eqn. (4).

464 Results of the reconstructed  $\widetilde{\delta J}_{[y,c,res]}$  as well as comparisons of these time-filtered  
 465 components to their counterparts from the forward model are shown in Fig. 4. The re-  
 466 constructed time series based on annual-means,  $\widetilde{\delta J}_y$  (Fig. 4a-b), capture well the sim-  
 467 ulated decadal change seen in  $\delta J_{fwd,y}$ . It has an apparent maximum  $\rho$  and PEV when  
 468 summing in time up to a lag of 36-months, but note that the change in correlation and  
 469 PEV is very small (0.01 and 1%). There appears to be a small annual cycle (at every  
 470 incremental 12-month lag) in both  $\rho$  and PEV, with a noticeable drop-off after 36-month  
 471 (Fig. 4b). One possible cause might be that 36-months is the time-scale where linear-  
 472 ity assumption holds and that beyond 36-months this assumption begins to break down.  
 473 Overall the correlation and PEV remain very high, nevertheless ( $\rho > 95\%$  and  $PEV >$   
 474  $92\%$ ).

475 There is a very small difference of 1–2% between using only wind stress and using  
 476 all atmospheric forcing variables for the reconstruction, implying that to first order winds  
 477 are the controlling factor, even at the multi-year time-scale, in setting the annual mean  
 478 anomalies (above the long-term mean flow of  $\sim 1$  Sv). For short lags the local winds dom-  
 479 inate, but for longer lags the net effect of winds is spread out over a much larger (basin-  
 480 scale) region, and we will return to this in Section 3.4.

481 The reconstructed time series based on monthly climatological values,  $\widetilde{\delta J}_c$  (Fig. 4c-  
 482 d), exhibit a pronounced degradation of  $\rho$  and PEV when using all atmospheric variables  
 483 (red line) after  $\sim 6$  month lag. An inspection of the reconstructed seasonal cycle of the  
 484 transport anomalies (Fig. 4c) shows that as more lagged sensitivities are used for the re-  
 485 construction, there is a noticeable shift in timing in the entire seasonal cycle, e.g., later

486 increase, later maximum, later decrease. As in the previous section, we speculate that  
 487 this degradation is due to non-linear effects of longwave and shortwave absorption in the  
 488 ocean, such that beyond  $\sim 5$  months the linearity assumption for buoyancy flux sensi-  
 489 tivities breaks down. What remains robust is that the sensitivity patterns from the first  
 490 two months (Fig. 2) capture  $> 98\%$  of the correlation and  $\sim 97\%$  of PEV. Even after  
 491 a 48 month lag, despite the degradation the PEV is still  $\leq 90\%$ . Overall, the reconstruc-  
 492 tion using only winds yields the highest correlation and PEV.

493 The remaining Bering Strait transport residual at sub-seasonal (monthly) time-scale,  
 494  $\delta J_{res}$ , is still well reconstructed (88% of PEV) by the local wind within four months prior,  
 495 with minimal improvement ( $\sim 1\%$ ) after the first month lag (Fig. 4f).

496 Overall, the time-filtered reconstructions reveal that adjoint sensitivity  $\partial J/\partial \Omega$  for  
 497 wind stress captures 95–98% of the variability of the full time series of the Bering Strait  
 498 transport anomaly at monthly to multi-year time-scales (Fig 4b,d,f). The degradation  
 499 in correlation between  $\widetilde{\delta J}$  and  $\delta J_{fwd}$  (Fig. 3b) is largely due to degradation in the re-  
 500 constructed seasonal cycle (Fig 4d). Despite the degradation, the correlation remains high,  
 501 with  $\sim 90\%$  of the variance captured at the seasonal time-scale. As the difference in the  
 502 reconstruction using all forcings and using only wind stresses is small, for the remain-  
 503 der of the analyses we will focus on reconstructions using only wind stress.

### 504 3.4 Decomposing $\widetilde{\delta J}(t)$ in space

505 Up to now, the reconstruction of  $\widetilde{\delta J}$  has been performed by integrating the effect  
 506 of winds over the entire globe (see eqn. 3). However, as discussed in Section 3.1, regions  
 507 near the strait and further away can contribute coherently or non-coherently at differ-  
 508 ent time lags. Fig. 5a shows a breakdown of contributions for the three most important  
 509 regions, which are chosen heuristically to include what our analysis shows are the major  
 510 regions of influence: (1) the Bering Sea Shelf (BeS), situated south of the strait with  
 511 dominantly positive sensitivity to northward wind stress; (2) the Gulf of Alaska (GoA),  
 512 situated further south of the strait with dominantly negative sensitivity to northward  
 513 wind stress; and (3) the Chukchi and East Siberian Seas (Ck+ESS) situated north of the  
 514 strait with positive sensitivity to northward wind stress.

515 The convolution restricted to these individual regions (Fig 5b) can be compared  
 516 with a global convolution (blue curve in Fig. 3 and Fig. 4). Only a limited period (2003–  
 517 2007) of the full time series (2002–2013) is presented here to simplify the visualization  
 518 of the regional contribution in individual years. With a few exceptions, regions BeS and  
 519 Ck+ESS contribute approximately equally in sign and magnitude to the total month-  
 520 to-month variation (each  $\sim 40\%$ ). Region GoA contributes very little ( $\sim 4\%$ ) to the to-  
 521 tal, and is therefore omitted from Fig. 5b for clarity. The dominance of the combined  
 522 BeS and Ck+ESS regions can be seen clearly in the scatter plots (Fig. 5c-d) for lags of  
 523 up to 12-months. Specifically, the green line (the sum of the BeS and Ck+ESS compo-  
 524 nents) is close to the grey lines, indicating that other terms are small. Summing contri-  
 525 butions up to 12-months lag does not significantly improve the reconstruction (i.e., com-  
 526 pare BeS plus Ck+ESS 1-month lag correlation of 0.91 with BeS plus Ck+ESS 12-month  
 527 lag correlation of 0.91).

528 Next, a more comprehensive spatial decomposition of the reconstruction is performed  
 529 to investigate the role of local versus far field influences in modifying the seasonal and  
 530 interannual variability. Seven regions were identified based on the magnitude of the ad-  
 531 joint sensitivity in both wind stress components (Fig. 6). Results show that all the re-  
 532 gions with significant influence are either over shallow high latitude shelves or along the  
 533 coastlines, and all are “upstream” of the Bering Strait in a Kelvin wave-propagation sense.  
 534 In the northern hemisphere, the coastally trapped Kelvin wave propagates with the coast  
 535 on its right, and thus the Bering Sea Shelf and the East Siberian Sea are both upstream  
 536 of the Bering Strait, and the Pacific Russian coast and the Arctic Alaskan Coast are both

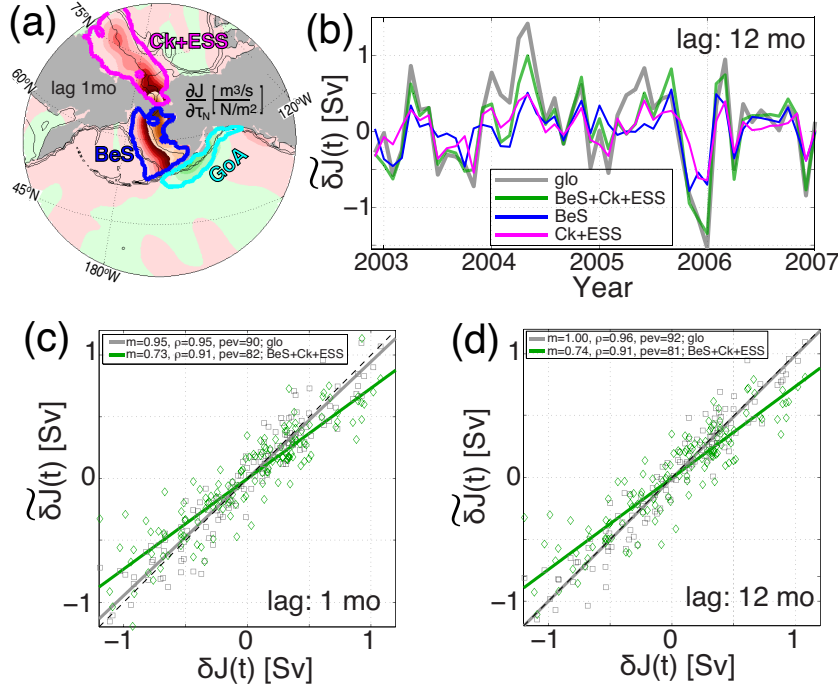


**Figure 5.** (a) Three regions that contribute the most to the Bering Strait transport anomalies at 1 month time lag: the Bering Sea Shelf (BeS), Gulf of Alaska (GoA), and the Chukchi and East Siberian Seas (Ck+ESS). (b) Reconstruction, using winds only, as a function of region of influence, including some combinations of regions (colors as per key) and the global sum (glo, grey line) for comparison. Scatter plot of the reconstructed  $\delta\tilde{J}$  and forward  $\delta J_{fwd}$  summed to lags of (c) 1-month and (d) 12-months. Legends in (c–d) show the fitted slope ( $m$ ), correlation ( $\rho$ ), and percentage of explained variance (PEV).

537 downstream of the strait in the Kelvin wave-propagation sense. The rest of the ocean  
 538 interior, labeled “rest”, generally has a smaller contribution than any of the seven iden-  
 539 tified regions. A hypothesis for the mechanisms that determine these regions will be pre-  
 540 sented in Section 4.

541 In the reconstruction of the seasonal cycle (Fig. 6b), while the Bering Sea and the  
 542 combined Chukchi and East Siberian Seas still give the largest contributions (each  $\sim 35\%$ ),  
 543 it is interesting to note the significant contributions ( $\sim 30\%$ ) of regions further north  
 544 of the strait such as the Laptev Sea (La), the Barents Sea (Ba), and the eastern North  
 545 Atlantic (Atl).

546 In the reconstruction of the interannual time-series (Fig. 6c), the Bering Sea and  
 547 the combined Chukchi and East Siberian Seas dominate most of the time, though oc-  
 548 casionally with opposite signs. Contributions from the Bering Sea Shelf are highly vari-  
 549 able in sign. Due to competition with other regions, they do not alone determine the sign  
 550 of the annual-mean anomaly. Overall, the Pacific-sector contributions to Bering Strait  
 551 transport originating from the Northwest Pacific (Pa) and Gulf of Alaska (GoA) are small,  
 552 ( $\sim 3\%$ ) except for the years 2005 and 2011 when they are large enough to offset the con-  
 553 tribution from the Bering Sea Shelf and result in a change of sign of the simulated an-  
 554 nual mean transport anomaly.

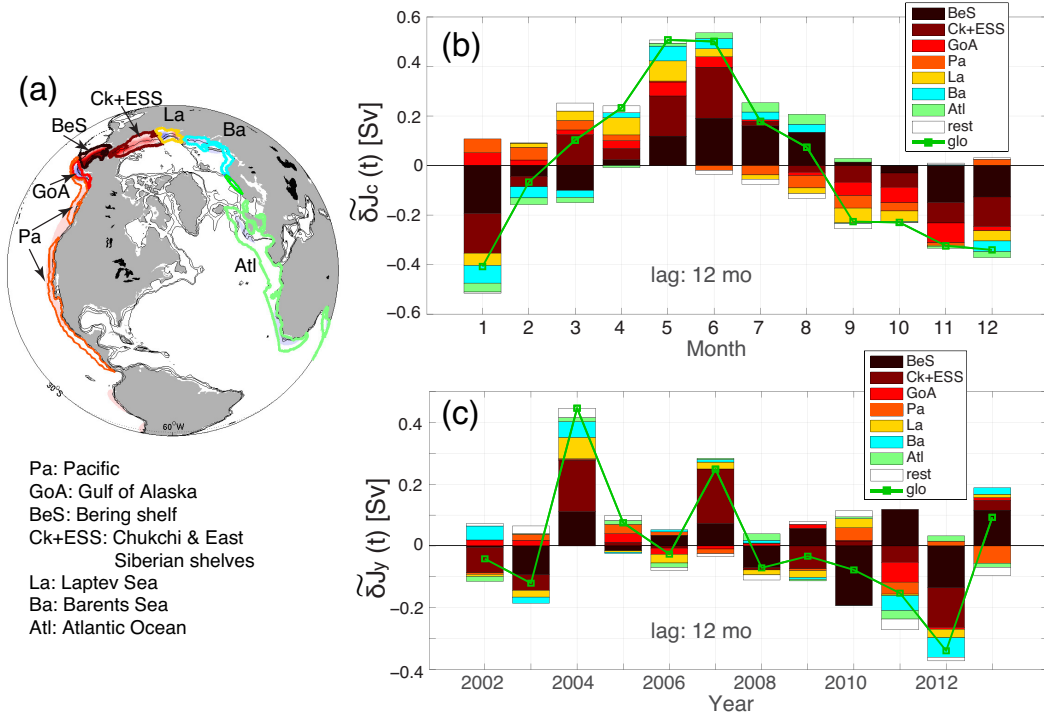


**Figure 6.** (a) Partition of regions of influence based on ocean regions and along important continental shelves. Reconstructions, using only  $\delta\tau_{[N,E]}$  of (b)  $\delta\bar{J}_c$  and (c)  $\delta\bar{J}_y$  as a function of regional contributions. In (b-c), “rest” refers to the rest of the ocean excluding those regions highlighted in (a), and “glo” is the global sum. Panel (a) also links region abbreviations to their geographical location.

555 During the two extreme years, 2004 and 2012, contributions from the combined La  
 556 and Ba are more prominent. Annual transport anomalies for these two years, in addi-  
 557 tion to 2007, are the primary factors determining the decline in the model annual trans-  
 558 ports between 2002–2013, and may have some bearing on the difference between the model  
 559 and observed trends.

560 The relationship between the extreme years and the regional contribution give in-  
 561 sight into the debate as to whether Bering Strait throughflow variability is forced from  
 562 the Pacific in the direction of the mean flow through the strait (which is northward) or  
 563 the Arctic/Atlantic. The traditional view of the dominance of Pacific origin forcing has  
 564 been recently challenged (Peralta-Ferriz & Woodgate, 2017). Fig. 7 splits the contribu-  
 565 tions shown in Fig. 6 into Pacific and Arctic/Atlantic components. Seasonally (Fig. 7b),  
 566 the results support the conclusion of Peralta-Ferriz and Woodgate (2017), that the sum-  
 567 mer transport variability is more strongly related to perturbations over the Arctic, al-  
 568 though the Pacific-forced component remains significant. During fall, forcing over the  
 569 Pacific is more important, although forcing over the Arctic still plays a significant role.  
 570 Interannually (Fig. 7c), both Pacific and Arctic/Atlantic forcings provide significant  
 571 contributions. Where their influences are coherent, extrema in transports are typically found  
 572 (2004, 2007, 2012). However, the Arctic/Atlantic contributions are generally larger and  
 573 more highly correlated with the total annual anomaly (correlation coefficient  $\rho(\delta\bar{J}_{Arctic/Atlantic}, \delta J_{fwd}) =$   
 574  $0.94$ , compared to  $\rho(\delta\bar{J}_{Pacific}, \delta J_{fwd}) = 0.74$ ), and can usually predict the sign of the  
 575 total anomaly (with the exception being the year 2010).

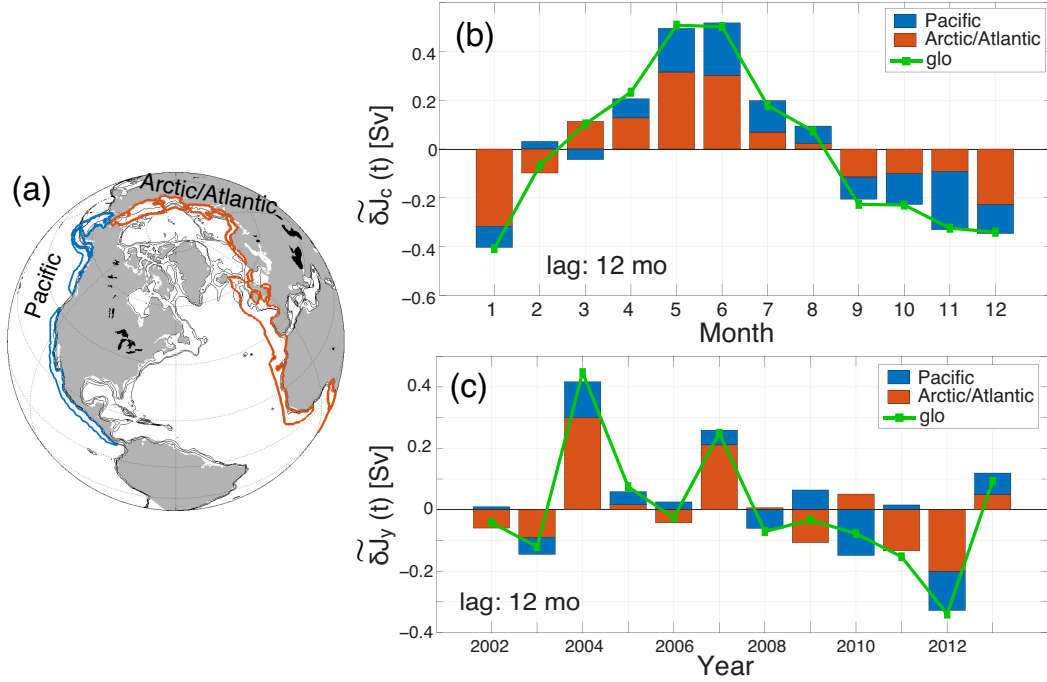


**Figure 7.** Same as Fig. 6, but partitioned in terms of contributions from the Pacific (south of the strait, blue) and Arctic/Atlantic sectors (north of the strait, orange).

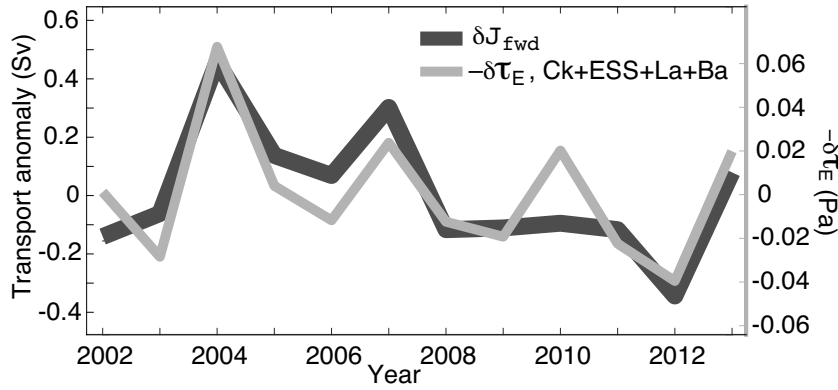


**Figure 8.** Minus eastward wind stress anomalies (light-gray, right y-axis) and transport anomalies (left y-axis) for the forward run ( $\delta J_{fwd}$ , thick dark gray).

576 We can go one step further and inspect the individual forcing anomalies in the eight  
 577 regions highlighted in Fig 6 to identify if any particular distribution of regional forcing  
 578 anomalies determine the three years of the transport extrema (2004, 2007, and 2012).  
 579 One strong correlation (correlation coefficient of 0.84) can be identified, as shown in Fig. 8,  
 580 between the combined  $\delta\tau_E$  for the combined regions Ck+ESS+La+Ba (grey) and the  
 581 annual Bering Strait transport anomalies  $\delta J$  (black line). Given the corresponding peaks  
 582 (positive and negative) of  $\delta\tau_E$  and  $\delta J$ , we can deduce that large  $\tau_E$  anomalies in the  
 583 regions north of the Bering Strait (Ck+ESS+La+Ba) are responsible for the extrema in  
 584 the model  $\delta J$ . To confirm this, we performed a series of perturbation experiments, in which  
 585 we replaced wind stress in years of extrema with that from the the prior years, and re-  
 586 strict the perturbed forcing to only within these regions. Our results (not shown) con-

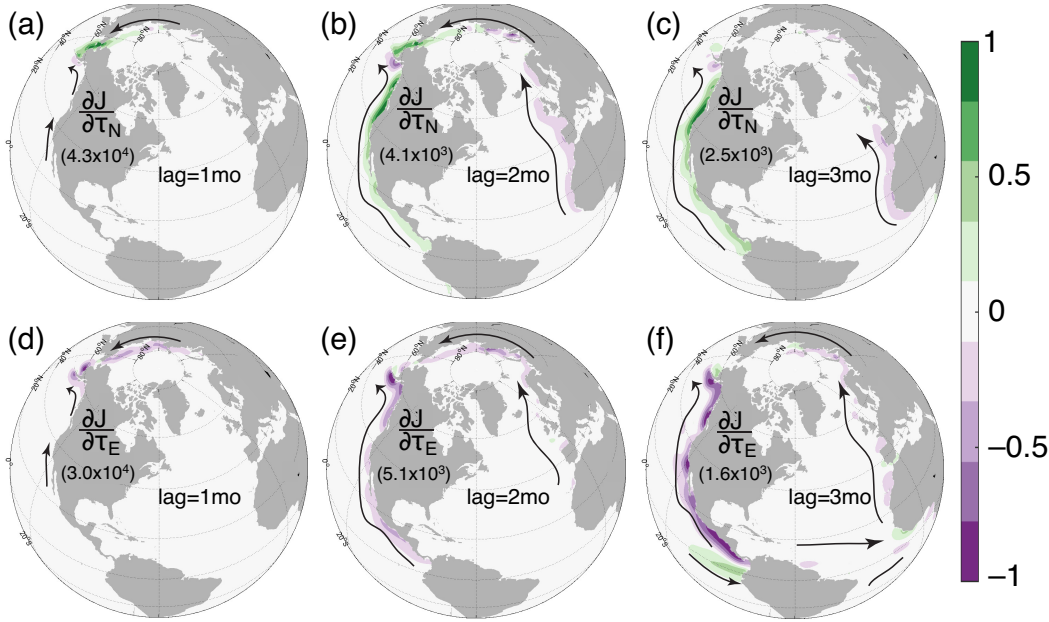


**Figure 9.** Normalized sensitivity (factor given on each plot) to  $\tau_N$  (a-c) and  $\tau_E$  (d-f) for lags of 1–3 months (columns). Arrows indicate direction of propagation of Kelvin and shelf waves. Geographical influence in time (reaching from the Pacific/Atlantic oceans in 2 months, and from the equator at 3 months lags) are consistent with wave phase speed estimates as discussed in the text. Note that scale factor varies by a factor of  $\sim 20$  across the different lags.

587 firm that wind stress anomalies in several key identified regions are primary controlling  
 588 factors in determining the transport results in the model. The result also underlines the  
 589 importance of improving the accuracy of wind stress in atmospheric reanalyses.

## 590 4 Discussion

### 591 4.1 Regions of Influence

592 Our work suggests the dominant forcing of Bering Strait transport anomalies to  
 593 be localized and with only limited time lag. Nevertheless, there are also remote, longer  
 594 timescale influences, as shown by Fig. 6. Continental shelf waves and coastally trapped  
 595 Kelvin waves have been suggested as important mechanisms for transferring perturbations  
 596 along coasts in general, (e.g. Brink, 1991; Heimbach et al., 2011; Pillar et al., 2016).  
 597 Using observations, atmospheric reanalyses, statistical analyses and idealized models, Danielson  
 598 et al. (2014) found evidence suggesting Kelvin and coastal shelf waves as playing an im-  
 599 portant role in influencing the Bering Strait throughflow variations. In our result, the  
 600 sensitivity patterns are consistent with propagation directions of such waves in the north-  
 601 ern hemisphere (i.e., with the coast to their right), with the important regions of influ-  
 602 ence all located upstream in the Kelvin/shelf wave-propagation sense of the strait. As  
 603 discussed in Section 2.1, both wavelengths and phase speeds of these waves may be mod-  
 604 ified due to numerical effects associated with grid-spacing aliasing and instability damp-  
 605 ing. The adjoint sensitivities shown here inherit such numerical modifications, and are  
 606 thus reflecting these modified coastal waves. Fig. 9 shows the sensitivities of  $\delta J$  to wind  
 607 stress, now highlighting the directions of Kelvin/shelf wave propagation that can con-  
 608 tribute to positive  $\delta J$ . For each subplot, the sensitivity is normalized by its maximum  
 609 magnitude at each corresponding lag to highlight the spatial distribution and time-scale

610 of propagation along the coastal regions. We ask next if the timescales are reasonable,  
 611 while keeping in mind the modified numerical representation of these waves.

612 Previous observational-based studies of multi-decadal sea surface height records along  
 613 the Siberian and Laptev Sea Shelves showed presence of shelf waves with phase veloc-  
 614 ities of 1.3 to 5.2 m/s and periods of less than 60 days associated with synoptic wind per-  
 615 turbations (Voinov & Zakharchuk, 1999). Further away in the Barents Sea and along the  
 616 Norwegian coast, numerical and theoretical calculations by Drivdal et al. (2016) support  
 617 evidence of the presence of coastal Kelvin waves and continental shelf waves generated  
 618 by atmospheric storms with a phase speed of 5–24 m/s and a period  $\sim 44$  hours. Esti-  
 619 mating the length of the east Siberian and Laptev Sea Shelves as  $\sim 4600$  km yields a timescale  
 620 of about 10–40 days for coastal shelf waves originated from these shelves to reach Bering  
 621 Strait. In the model, sensitivities associated with the expected damped phase speeds are  
 622 seen with lags within 1 month (Fig. 9a), which can be interpreted as consistent with the  
 623 observed timing of  $\sim 10+$  days for fast shelf waves plus numerically induced delay. Sim-  
 624 ilarly, the additional distance to traverse along the coast in the Barents and Nordic Seas  
 625 of 8000 km at wave phase speeds 5–24 m/s yields an additional 4–20 days. Thus, for fast  
 626 waves, the theoretical travel time from south of the Nordic Seas to Bering Strait is  $\sim 14$  days.  
 627 Model sensitivities indicate that it takes less than two months for waves which originated  
 628 along these coastal regions to reach the Bering Strait (Fig. 9b). Again, considering the  
 629 expected damped phase velocities suggests shelf waves in the faster range associated with  
 630 transit time  $\sim 14+$  days plus delay as the likely mechanism.

631 Within three months, sensitivities can be traced to the equatorial Kelvin wave-guide  
 632 paths (wave phase speed  $\sim 1$ –3 m/s estimated by Eriksen et al., 1983 over a distance  $\sim 7300$  km,  
 633 yielding a transit time of 28–84 days, or twice the duration if we assume a 50% under-  
 634 estimation of the phase velocity in the model) in both the Pacific and Atlantic Oceans  
 635 (Heimbach et al., 2011). As information is more dispersed spatially, the magnitude of  
 636 sensitivities decreases such that the total contributions of all regions to wind perturba-  
 637 tions at this lag only contribute  $\sim 1\%$  to the total Bering Strait transport. Note that the  
 638 high or low sensitivity by itself does not solely determine the magnitude of the contri-  
 639 bution to transport  $\delta J$  from that region, since the final contribution to transport depends  
 640 on the sum through various lags of the product of sensitivity and the forcing anomaly.

641 In terms of wind stress magnitude and direction, as indicated by the color scale in  
 642 Fig. 9, northwestward wind stress (positive  $\tau_N$ , negative  $\tau_E$ ) along the coast in the Pa-  
 643 cific contribute primarily to positive increase in  $\delta \tilde{J}$  at Bering Strait. Similarly, along the  
 644 coast of the East Siberian and Laptev Seas, northwestward wind stress gives positive  $\delta \tilde{J}$ .  
 645 At further distance from the strait in the Arctic/Atlantic sector, along the coast in the  
 646 Barents and Nordic Seas and in the eastern margin of the Atlantic Ocean, southwest-  
 647 ward wind stress contribute to positive  $\delta \tilde{J}$ . This is consistent with results from Peralta-  
 648 Ferriz and Woodgate (2017) which show that winds that invoke onshore (offshore) Ek-  
 649 man flow in the Bering+Pacific sector (Arctic + Barents + Nordic + Atlantic sector)  
 650 are related to positive flow anomalies at the strait.

## 651 4.2 The Effect of Precipitation

652 The majority of work in this paper has focused on the impacts of wind stress anoma-  
 653 lies on the flow variations through the strait, as that was found to be the greatest driver  
 654 in the adjoint experiments performed. The method, however, allows us to examine the  
 655 impact of other forcings as well – e.g., precipitation which is also hypothesized to be a  
 656 driver of the Bering Strait throughflow variability (Stigebrandt, 1984).

657 Fig. 10 shows the sensitivity of the Bering Strait transport anomaly to precipita-  
 658 tion perturbations for lags ranging from 1 month to 10 years. Summing these shows the  
 659 total contribution to Bering Strait flow variability to be small (order of 0.01 Sv). Nev-  
 660 ertheless, the patterns are themselves interesting. At 1 month lag, Bering Strait flow is

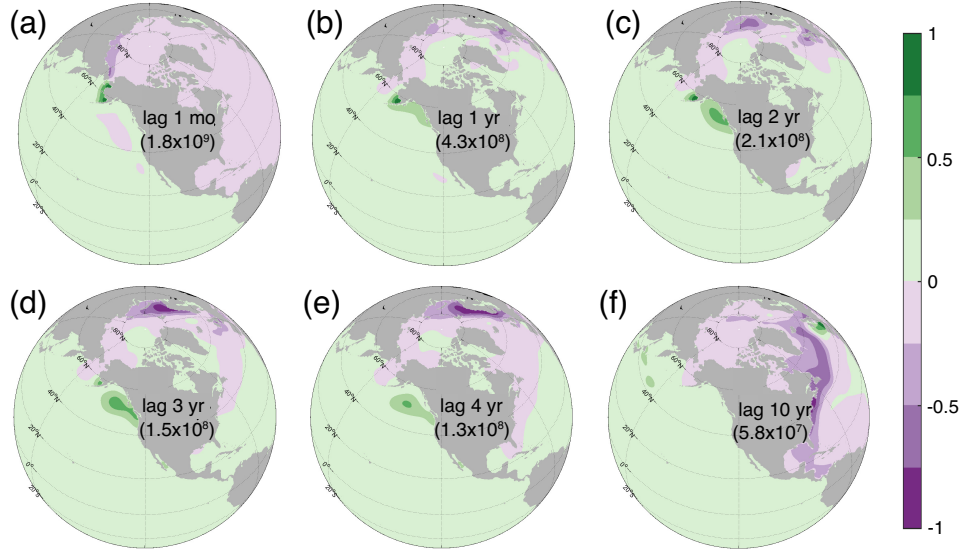


**Figure 10.** (a) Normalized adjoint sensitivity to precipitation (positive precipitation implies adding freshwater to the ocean) for time lags from 1 month to 10 years. The normalization factor is the maximum magnitude of sensitivity at each lag and is given on each plot. Note that the normalization factor varies by a factor of  $\sim 30$  across the plots.

661 enhanced by positive net precipitation over the Bering Sea Shelf and negative net pre-  
 662 cipitation over the east Siberian Sea. This pattern enhances the steric sea surface slope  
 663 through the strait, mechanically increasing northward flow, as per the steric driving  
 664 of the flow due to the global freshwater cycle as suggested by Stigebrandt (1984). At longer  
 665 lags of 1–4 years, the region of sensitivity to positive precipitation is further south (along  
 666 the Alaskan Coast) while the region where negative precipitation enhances the flow now  
 667 extends further along the Russian coast and into the Bering Sea. Note that these lags  
 668 are much larger than the few-month lags for wind stress forcings, indicative of the dif-  
 669 ference between the wave phase speeds of a few m/s and mean ocean circulation speeds  
 670 of order of a few cm/s.

671 Precipitation influences emerge along the Gulf Stream paths in the North Atlantic  
 672 after 3 years (Fig. 10d-f) and along the Kuroshio path in the North Pacific after 4 years  
 673 (Fig. 10e-f). In general, the sign of the sensitivity is consistent with the steric “pressure  
 674 head” hypothesis (Stigebrandt, 1984) that negative (positive) precipitation anomalies  
 675  $\delta P$  into the Atlantic (Pacific) Ocean would increase the steric sea surface height differ-  
 676 ence between the two oceans and promote increased in  $\delta J$  at the strait. However, given  
 677 that the magnitude of  $\partial J / \partial P$  of  $O(10^9)$  ( $\text{m}^3/\text{s})/(\text{m}/\text{s})$  and that  $\delta P$  is of the order  $O(10^{-8})$  m/s,  
 678  $\delta J_P$  is of the order  $O(10^1)$   $\text{m}^3/\text{s}$  or  $(10^{-5})$  Sv which is significantly smaller than contri-  
 679 butions from wind stress, we conclude that these patterns, though interesting, are not  
 680 of much relevance, and advective/wind-driven effects are a much larger forcing of the Bering  
 681 Strait throughflow than the steric term, at least on timescales of months to years, as De Boer  
 682 and Nof (2004a, 2004b) have suggested. Note that since we are considering anomalies,  
 683 we cannot draw direct conclusions about the forcing of the **mean** of the Bering Strait  
 684 transport, which may still have a significant steric contribution.

## 5 Conclusions

The ECCOv4r2 forward and adjoint models were used to investigate the mechanisms controlling the variability of the Bering Strait throughflow. Adjoint sensitivities show that the model’s Bering Strait transport anomaly is controlled primarily by the wind stress on short time-scales of order 0–5 months, with the percentage of explained monthly variance of the flow being  $\sim 90\%$  and  $92\%$  within the first month and the first five months, respectively. Other atmospheric forcing terms (precipitation, radiative fluxes, water vapor content, air temperature) have negligible ( $< 1\%$ ) influence on both short (monthly) and long (interannual) variability.

Spatial decomposition indicates that on short time scales (monthly) winds over the Bering Shelf and the combined Chukchi and East Siberian regions are the most significant drivers. Each region contributes approximately equal amounts in magnitudes to the net transport anomalies ( $\sim 40\%$  each), with the combined Chukchi and East Siberian regions being slightly more influential. Sensitivity patterns indicative of coastally trapped adjoint wave propagation lead us to hypothesize that continental shelf waves and coastally-trapped waves are the dominant mechanisms for propagating information from upstream (in the Kelvin wave-propagation sense) to the strait. Further support for this hypothesis comes from a reasonable match of timescales of propagation of influences with wave phase speed estimates from the literature and findings from prior work by Danielson et al. (2014) and others, after potential numerical damping of the model’s fast waves is taken into account.

Including wind-stress influence from regions further away from the strait in the reconstruction yields a similar conclusion that the Bering Sea Shelf, the Chukchi Sea, and the East Siberian Sea remain the dominant drivers of the Bering Strait flow variability ( $80\%$  combined), with additional contribution of influences from the Barents and Nordic Seas, the eastern Pacific Ocean and eastern Atlantic Ocean (Fig. 6). These far field influences contribute  $\sim 20\%$  of the monthly-scale variability (Fig. 5b) and  $\sim 30\%$  of the seasonal variability (Fig. 6b).

To address the long standing question as to whether the flow variability is driven from the Pacific or the Arctic/Atlantic sector, influences of forcing anomalies from these two regions were compared. Results show that both sectors are important, and that extrema in transports occur when their influences act in concert. Interestingly, the Arctic/Atlantic forcings are better predictors of anomalous flow than those over the Pacific (correlation coefficient  $\rho(\delta\widetilde{J}_{Arctic/Atlantic}, \delta J_{fw}) = 0.94$  compare to  $\rho(\delta\widetilde{J}_{Pacific}, \delta J_{fw}) = 0.74$ ). An important conclusion is the recognition that the Arctic shelves act as efficient conduits and play a substantial role in determining the Bering Strait flow variability. Our results support previous findings (De Boer & Nof, 2004a, 2004b) of the importance of basin-scale winds (Peralta-Ferriz & Woodgate, 2017) in driving the Bering Strait transport variability. They also show that the contribution of net freshwater fluxes (precipitation and runoff minus evaporation) contributes very little ( $< 1\%$ ) to the transport variability.

In contrast to previous work, which is based on simple theoretical or statistical models, our results are based on the use of the dynamically and kinematically consistent state-estimation framework and the detailed analysis of adjoint model-derived sensitivities to conduct dynamical attributions. These results yield more physical insight than is conventionally obtained from purely statistical methods. Our findings of the impact of local and far field forcings on the flow substantially advance our understanding of the mechanisms driving transport variability at the Bering Strait. Another key finding is the importance of the Arctic (especially the Chukchi and the East Siberian and Laptev Seas) on the flow variability, contrasting the prior assumptions that the flow is driven primarily from south of the strait. Lastly, the short-term and localized response of the strait

736 transport anomalies to the forcing suggests some predictive skill if sufficiently accurate  
737 wind stress fields, especially in the Arctic, are available.

## Acknowledgments

This work was supported by NSF OPP grants 1304050 and 1603903, and by NSF Arctic Observing Network grants PLR-1304052 and PLR 1758565. Additional support for PH came from a JPL/Caltech subcontract for the “Estimating the Circulation and Climate of the Ocean” project. The Bering Strait mooring data are freely available via the Bering Strait Observing Network website ([psc.apl.washington.edu/BeringStrait.html](http://psc.apl.washington.edu/BeringStrait.html)) and the permanent US oceanographic data archives at the National Centers for Environmental Information ([www.nodc.noaa.gov](http://www.nodc.noaa.gov)). The ECCOV4r2 model setup used in this work can be accessed from public repositories and permanent archives (Campin et al., 2019; Forget, 2016a, 2016b, 2018). Adjoint code was generated using the TAF software tool, created and maintained by FastOpt GmbH (<http://www.fastopt.com/>). We thank two anonymous reviewers for comments that greatly improved the manuscript.

## References

- Adcroft, A., Campin, J., Dutkiewicz, S., Evangelinos, C., Ferreira, D., Forget, G., . . . Molod, A. (2018). *MITgcm user manual*. doi: 1721.1/117188
- Adcroft, A., & Campin, J.-M. (2004). Rescaled height coordinates for accurate representation of free-surface flows in ocean circulation models. *Ocean Modelling*, 7(2004), 269–284. doi: 10.1016/j.ocemod.2003.09.003
- Adcroft, A., Hill, C., & Marshall, J. (1997). Representation of topography by shaved cells in a height coordinate ocean model. *Mon. Wea. Rev.*, 125, 2293–2315.
- Arrigo, K. R. (2014). Sea ice ecosystems. *Annual Review of Marine Science*, 6(1), 439-467. (PMID: 24015900) doi: 10.1146/annurev-marine-010213-135103
- Arrigo, K. R., Perovich, D. K., Pickart, R. S., Brown, Z. W., van Dijken, G. L., Lowry, K. E., . . . Swift, J. H. (2012). Massive phytoplankton blooms under Arctic sea ice. *Science*. doi: 10.1126/science.1215065
- Brink, K. (1991). Coastal-trapped waves and wind-driven currents over the continental shelf. *Annu. Rev. Fluid Mech.*, 23, 389–412.
- Campin, J.-M., Adcroft, A., Hill, C., & Marshall, J. (2004). Conservation of properties in a free-surface model. *Ocean Modelling*, 6, 221–244. doi: 10.1016/S1463-5003(03)00009-X
- Campin, J.-M., Heimbach, P., Losch, M., Forget, G., Hill, E., Adcroft, A., . . . McRae, A. T. T. (2019). *MITgcm/MITgcm: checkpoint67m*. Zenodo. doi: 10.5281/zenodo.3492298
- Casulli, V., & Cattani, E. (1994). Stability, accuracy, and efficiency of a semi-implicit method for three-dimensional shallow water flow. *Computers Math. Applic.*, 27(4), 99–112.
- Cavalieri, D. J., Crawford, J., Drinkwater, M. R., Eppler, D., Farmer, L. D., Jentz, R. R., & Wackerman, C. C. (1991). Aircraft active and passive microwave validation of sea ice concentration from the DMSP SSM/I. *Journal of Geophysical Research*, 96(C12), 21989–22009.
- Chaudhuri, A., Ponte, R., Forget, G., & Heimbach, P. (2013). A comparison of atmospheric reanalysis surface products over the ocean and implications for uncertainties in air-sea boundary forcing. *J. Climate*, 26, 153–170. doi: JCLI-D-12-00090.1
- Chaudhuri, A., Ponte, R., & Nguyen, A. (2014). A comparison of atmospheric reanalysis products for the Arctic Ocean and implications for uncertainties in air-sea fluxes. *J. Climate*, 27(14), 5411–5421. doi: <http://dx.doi.org/10.1175/JCLI-D-13-00424.1>
- Coachman, L., & Aagaard, K. (1966). On the water exchange through Bering Strait. *Limnology and Oceanogr.*, 11(1), 44–59. doi: 10.4319/lo.1966.11.1.0044
- Danielson, S. L., Weingartner, T. J., Hedstrom, K. S., Aagaard, K., Woodgate, R. A., Chuchitser, E., & Stabenro, P. J. (2014). Coupled wind-forced controls of the Bering-Chukchi shelf circulation and the Bering Strait through-

- 791 flow: Ekman transport, continental shelf waves, and variations of the Pacific-  
 792 Arctic sea surface height gradient. *Progress in Oceanogr.*, *125*, 40–61. doi:  
 793 <http://dx.doi.org/10.1016/j.pocean.2014.04.006>
- 794 De Boer, A., & Nof, D. (2004a). The Bering Strait’s grip on the northern hemi-  
 795 sphere climate. *Deep-Sea Res., Part I*, *51*(10), 1347–1366. doi: 10.1016/j.dsr  
 796 .2004.05.003
- 797 De Boer, A., & Nof, D. (2004b). The exhaust valve of the North Atlantic. *J. Cli-  
 798 mate*, *17*(3), 417–422. doi: 10.1175/1520-0442
- 799 Dee, D. P., Uppala, S. M., Simmons, A. J., Berrisford, P., Poli, P., Kobayashi, S., . . .  
 800 Vitart, F. (2011). The ERA-Interim reanalysis: configuration and performance  
 801 of the data assimilation system. *Q. J. R. Meteorol. Soc.*, *137*(656), 553–597.  
 802 doi: 10.1002/qj.828
- 803 Drivdal, M., Weber, J., & Debernard, J. (2016). Dispersion relation for continental  
 804 shelf waves when the shallow shelf part has an arbitrary width: Application to  
 805 the shelf west of Norway. *Journal of Physical Oceanography*, *46*(2), 537–549.  
 806 doi: 10.1175/JPO-D-15-0023.1
- 807 Eriksen, C., Blumenthal, M., Hayes, S., & Ripa, P. (1983). Wind-generated equa-  
 808 torial Kelvin waves observed across the Pacific Ocean. *Journal of Physical  
 809 Oceanography*, *13*, 1622–1640.
- 810 Fenty, I., & Heimbach, P. (2013). Coupled sea ice-ocean state estimation in the  
 811 Labrador Sea and Baffin Bay. *J. Phys. Ocean.*, *43*(6), 884–904. doi: 10.1175/  
 812 JPO-D-12-065.1
- 813 Fenty, I., Menemenlis, D., & Zhang, H. (2015). Global coupled sea ice-ocean state  
 814 estimate. *Clim. Dyn.* doi: 10.1007/s00382-015-2796-6
- 815 Forget, G. (2016a). *ECCO version 4 release 2 inputs: model initialization*. Harvard  
 816 Dataverse. doi: 10.7910/DVN/7XYXSF
- 817 Forget, G. (2016b). *ECCO version 4 release 2 inputs: surface forcing fields*. Harvard  
 818 Dataverse. doi: 10.7910/DVN/9WYSZF
- 819 Forget, G. (2018). *gaelforget/eccov4: Documentation updates*. Zenodo. doi: 10.5281/  
 820 zenodo.1211363
- 821 Forget, G., Campin, J. M., Heimbach, P., Hill, C. N., Ponte, R. M., & Wunsch, C.  
 822 (2015). ECCO version 4: an integrated framework for non-linear inverse mod-  
 823 eling and global ocean state estimation. *Geosci. Model Dev.*, *8*, 3071–3104. doi:  
 824 10.5194/gmd-8-3071-2015
- 825 Fukumori, I., Heimbach, P., Ponte, R. M., & Wunsch, C. (2018). A dynamically con-  
 826 sistent, multi-variable ocean climatology. *Bulletin of the American Meteorologi-  
 827 cal Society*. doi: 10.1175/BAMS-D-17-0213.1
- 828 Fukumori, I., Wang, O., Llovel, W., Fenty, I., & Forget, G. (2015). A near-uniform  
 829 fluctuation of ocean bottom pressure and sea level across the deep ocean basins  
 830 of the Arctic Ocean and the Nordic Seas. *Progress in Oceanography*, *134*(C),  
 831 152–172.
- 832 Griffiths, S. D. (2013). Kelvin wave propagation along straight boundaries in C-grid  
 833 finite-difference models. *Journal of Computational Physics*, *255*, 639–659. doi:  
 834 <http://dx.doi.org/10.1016/j.jcp.2013.08.040>
- 835 Heimbach, P., Fukumori, I., Hill, C. N., Ponte, R. M., Stammer, D., Wunsch, C., . . .  
 836 Zhang, H. (2019). Putting it all together: Adding value to the global ocean  
 837 and climate observing systems with complete self-consistent ocean state and  
 838 parameter estimates. *Frontiers in Marine Science*, *6*, 769–10.
- 839 Heimbach, P., Menemenlis, D., Losch, M., Campin, J., & Hill, C. (2010). On the  
 840 formulation of sea-ice models. Part 2: Lessons from multi-year adjoint sea-ice  
 841 export sensitivities through the Canadian Arctic Archipelago. *Ocean Modeling*,  
 842 *33*(1–2), 145–158. doi: 10.1016/j.ocemod.2010.02.002
- 843 Heimbach, P., Wunsch, C., Ponte, R. M., Forget, G., Hill, C., & Utke, J. (2011).  
 844 Timescales and regions of the sensitivity of Atlantic meridional volume  
 845 and heat transport: Toward observing system design. *Deep Sea Research*

- 846 *Part II: Topical Studies in Oceanography*, 58(17-18), 1858–1879. doi:  
847 10.1016/j.dsr2.2010.10.065
- 848 Hsieh, W. W., Davey, M. K., & Wajswicz, R. C. (1983). The free Kelvin wave in  
849 finite-difference numerical models. *J. Phys. Oceanogr.*, 13, 1383–1397.
- 850 Hu, A., & Meehl, G. (2005). Bering Strait throughflow and the thermohaline circula-  
851 tion. *Geophys. Res. Lett.*, 32(L24610). doi: 10.1029/2005GL024424
- 852 Hu, A., Meehl, G., Han, W., Timmermann, A., Otto-Bliesner, B., Liu, Z., . . . Wu,  
853 B. (2012). Role of the Bering Strait on the hysteresis of the ocean conveyor  
854 belt circulation and glacial climate stability. *Proceedings of the National  
855 Academy of Sciences of the United States of America*, 109(17), 6417–6422. doi:  
856 10.1073/pnas.1116014109
- 857 Kalnay, E., Kanamitsu, M., Kistler, R., Collins, W., Deaven, D., Gandin, L.,  
858 . . . Reynolds, R. (1996). The NCEP/NCAR 40-Year reanalysis project.  
859 *Bulletin of the American Meteorological Society*, 77(3), 437–471. doi:  
860 10.1175/1520-0477(1996)077<0437:TNYRP>2.0.CO;2
- 861 Kawai, Y., Osafune, S., Masuda, S., & Komuro, Y. (2018). Relations between  
862 salinity in the northwestern Bering Sea, the Bering Strait throughflow and sea  
863 surface height in the Arctic Ocean. *Journal of Oceanography*, 74, 239–261. doi:  
864 <https://doi.org/10.1007/s10872-017-0453-x>
- 865 Kinney, J. C., Maslowski, W., Aksenov, Y., de Cuevas, B., Nguyen, A., Osinski,  
866 R., . . . Zhang, J. (2014). On the flow through Bering Strait: a synthesis of  
867 model results and observations. In J. Grebmeier & W. Maslowski (Eds.), (pp.  
868 167–198). Dordrecht: Springer Dordrecht.
- 869 Kobayashi, S., Ota, Y., Harada, Y., Ebata, A., Moriya, M., Onoda, H., . . . Taka-  
870 hashi, K. (2015). The JRA-55 reanalysis: General specifications and basic  
871 characteristics. *Journal of the Meteorological Society of Japan*, 93(1), 5–48.
- 872 Kurihara, Y. (1965). On the use of implicit and iterative methods for the time inte-  
873 gration of the wave equation. *Monthly Weather Review*, 93(1), 33–46.
- 874 Lammers, R. B., & Shiklomanov, A. I. (2001). Assessment of contemporary Arctic  
875 river runoff based on observational discharge records. *J. Geophys. Res.*,  
876 106(D4), 3321.
- 877 Marshall, J., Adcroft, A., Hill, C., Perelman, L., & Heisey, C. (1997). A finite-  
878 volume, incompressible Navier Stokes model for studies of the ocean on parallel  
879 computers. *J. Geophys. Res.*, 102, 5753–5766.
- 880 Nguyen, A. T., Menemenlis, D., & Kwok, R. (2011). Arctic ice-ocean simulation  
881 with optimized model parameters: approach and assessment. *J. Geophys. Res.*,  
882 116. doi: 10.1029/2010JC006573
- 883 Onogi, K., Tsutsui, J., Koide, H., Sakamoto, M., Kobayashi, S., Hatsushika, H.,  
884 . . . Taira, R. (2007). The JRA-25 reanalysis. *J. Meteor. Soc. Japan*, 85(3),  
885 369–432.
- 886 Peralta-Ferriz, A. C., & Woodgate, R. A. (2017). The dominant role of the East  
887 Siberian Sea in driving the oceanic flow through the Bering Strait - Conclu-  
888 sions from GRACE ocean mass satellite data and in situ mooring observations  
889 between 2002 and 2016. *Geophysical Research Letters*, 44, 11,472–11,481. doi:  
890 10.1002/2017GL075179
- 891 Pillar, H., Heimbach, P., Johnson, H., & Marshall, D. (2016). Dynamical attribution  
892 of recent variability in Atlantic overturning. *J. Clim.*, 29, 3339–3352. doi: 10  
893 .1175/JCLI-D-15-0727.1
- 894 Roemmich, D., Johnson, G., Riser, S., Davis, R., Gilson, J., Owens, W., . . . Ig-  
895 naszewski, M. (2009). The Argo program: Observing the global ocean with  
896 profiling floats. *Oceanography*, 22(2), 34–44. doi: 10.5670/oceanog.2009.36
- 897 Schwab, D. J., & Beletsky, D. (1998). Propagation of Kelvin waves along irregu-  
898 lar coastlines in finite-difference models. *Advances in Water Resources*, 22(3),  
899 239–245.
- 900 Serreze, M. C., Barrett, A. P., Slater, A. G., Steele, M., Zhang, J., & Trenberth,

- 901 K. E. (2007). The large-scale energy budget of the Arctic. *J. Geophys. Res.*,  
 902 *112*(C11122). doi: 10.1029/2006JD008230
- 903 Serreze, M. C., Barrett, A. P., Slater, A. G., Woodgate, R. A., Aagaard, K., Lam-  
 904 mers, R. B., ... Lee, C. M. (2006). The large-scale freshwater cycle of the  
 905 Arctic. *J. Geophys. Res.*, *111*(C11010). doi: 10.1029/2005JC003424
- 906 Serreze, M. C., Crawford, A. D., Stroeve, J., Barrett, A. P., & Woodgate, R. A.  
 907 (2016). Variability, trends, and predictability of seasonal sea ice retreat and  
 908 advance in the Chukchi Sea. *J. of Geophys. Res.*. doi: 10.1002/2016jc011977
- 909 Shiklomanov, A. I., Yakovleva, T. I., Lammers, R. B., Karasev, I. P., Vörösmarty,  
 910 C. J., & Linder, E. (2006). Cold region river discharge uncertainty—estimates  
 911 from large Russian rivers. *Journal of Hydrology*, *326*(1-4), 231–256.
- 912 Smith, T., & Heimbach, P. (2018). Atmospheric origins of variability in the South  
 913 Atlantic meridional overturning circulation. *Journal of Climate*, *32*, 1483–  
 914 1500. doi: <https://doi.org/10.1175/JCLI-D-18-0311.1>
- 915 Stammer, D. (2005). Adjusting internal model errors through ocean state estima-  
 916 tion. *J. Phys. Oceanogr.*, *35*(6), 1143–1153.
- 917 Stammer, D., Balmaseda, M., Heimbach, P., Köhl, A., & Weaver, A. (2016). Ocean  
 918 data assimilation in support of climate applications: Status and perspectives.  
 919 *Annu. Rev. Mar. Sci.*, *8*(1), 491–518. doi: 10.1146/annurev-marine-122414-  
 920 -034113
- 921 Steele, M., & Ermold, W. (2007). Steric sea level change in the Northern Seas. *Jour-  
 922 nal of Climate*, *20*, 403–417.
- 923 Stigebrandt, A. (1984). The North Pacific: a global-scale estuary. *J. Phys.  
 924 Oceanogr.*, *14*(2), 464–470.
- 925 Toole, J., Krishfield, R., Proshutinsky, A., Ashjian, C., Doherty, K., Frye, D., ...  
 926 Shanahan, T. (2006). Ice-tethered profilers sample the upper Arctic Ocean.  
 927 *EOS Trans. AGU*, *87*(41), 434–3.
- 928 Toulany, B., & Garrett, C. (1984). Geostrophic control of fluctuating barotropic flow  
 929 through straits. *Journal of Physical Oceanography*, *14*(4), 649–655. doi: 10  
 930 .1175/1520-0485(1984)014<0649:GCOFBF>2.0.CO;2
- 931 Uppala, S. M., Kallberg, P. W., Simmons, A. J., Andrae, U., Bechtold, V. D. C.,  
 932 Fiorino, M., ... Woollen, J. (2005). The ERA-40 re-analysis. *Quarterly  
 933 Journal of the Royal Meteorological Society*, *131*(612), 2961–3012. doi:  
 934 10.1256/qj.04.176
- 935 Voinov, G., & Zakharchuk, E. (1999). Large-Scale variations of sea level in the  
 936 Laptev Sea. In H. Kassens et al. (Eds.), (pp. 25–36). Berlin, Heidelberg:  
 937 Springer Berlin Heidelberg.
- 938 Wadley, M. R., & Bigg, G. R. (2002). Impact of flow through the Canadian  
 939 Archipelago and Bering Strait on the North Atlantic and Arctic circulation:  
 940 An ocean modelling study. *Quarterly Journal of the Royal Meteorological So-  
 941 ciety*, *128*(585), 2187–2203. Retrieved from [http://dx.doi.org/10.1256/  
 942 qj.00.35](http://dx.doi.org/10.1256/qj.00.35) doi: 10.1256/qj.00.35
- 943 Walsh, J., Dieterle, D., Muller-Karger, F., Aagaard, K., Roach, A., Whitlege, T., &  
 944 Stockwell, D. (1997). CO<sub>2</sub> cycling in the coastal ocean. II. Seasonal organic  
 945 loading of the Arctic Ocean from source waters in the Bering Sea. *Continental  
 946 Shelf Research*, *17*(1), 1–36.
- 947 Weingartner, T., Danielson, S., & Royer, T. (2005). Freshwater variability and pre-  
 948 dictability in the Alaska Coastal Current. *Deep Sea Research II*, *52*, 169–191.
- 949 Woodgate, R. A. (2018). Increases in the Pacific inflow to the Arctic from 1990  
 950 to 2015, and insights into seasonal trends and driving mechanisms from year-  
 951 round Bering Strait mooring data. *Progress in Oceanography*, *160*, 124–154.  
 952 doi: <https://doi.org/10.1016/j.pocean.2017.12.007>
- 953 Woodgate, R. A., Aagaard, K., & Weingartner, T. J. (2005a). Monthly tempera-  
 954 ture, salinity, and transport variability of the Bering Strait through flow. *Geo-  
 955 phys. Res. Lett.*, *32*(L04601). doi: 10.1029/2004GL021880

- 956 Woodgate, R. A., Aagaard, K., & Weingartner, T. J. (2005b). A year in the  
957 physical oceanography of the Chukchi Sea: Moored measurements from  
958 autumn 1990-1991. *Deep-Sea Res., Part II*, 52(24-26), 3116-3149. doi:  
959 10.1016/j.dsr2.2005.10.016
- 960 Woodgate, R. A., Aagaard, K., & Weingartner, T. J. (2006). Interannual changes in  
961 the Bering Strait fluxes of volume, heat and freshwater between 1991 and 2004.  
962 *Geophys. Res. Lett.*, 33(L15609), 10.1029/2006GL026931.
- 963 Woodgate, R. A., Stafford, K. J., & Prahl, F. G. (2015). A synthesis of year-round  
964 interdisciplinary mooring measurements in the Bering Strait (1990-2014)  
965 and the RUSALCA years (2004-2011). *Oceanography*, 28(3), 46-67. doi:  
966 10.5670/oceanog.2015.57
- 967 Woodgate, R. A., Weingartner, T., & Lindsay, R. (2010). The 2007 Bering Strait  
968 oceanic heat flux and anomalous Arctic sea-ice retreat. *Geophys. Res. Lett.*,  
969 37(L01602). doi: 10.1029/2009GL041621
- 970 Woodgate, R. A., Weingartner, T., & Lindsay, R. (2012). Observed increases in  
971 Bering Strait oceanic fluxes from the Pacific to the Arctic from 2001 to 2011  
972 and their impacts on the Arctic Ocean water column. *Geophys. Res. Lett.*,  
973 39(L24603). doi: 10.1029/2012GL054092
- 974 Wunsch, C., & Heimbach, P. (2007). Practical global oceanic state estimation. *Phys-*  
975 *ica D: Nonlinear Phenomena*, 230(1-2), 197-208. doi: 10.1016/j.physd.2006.09  
976 .040
- 977 Wunsch, C., & Heimbach, P. (2013). Dynamically and kinematically consistent  
978 global ocean circulation and ice state estimates. In *Ocean circulation and cli-*  
979 *mate: A 21st century perspective* (pp. 553-579). Elsevier Ltd. doi: 10.1016/  
980 B978-0-12-391851-2.00021-0